J. Fluid Mech. (2024), *vol*. 979, A25, doi:10.1017/jfm.2023.1069

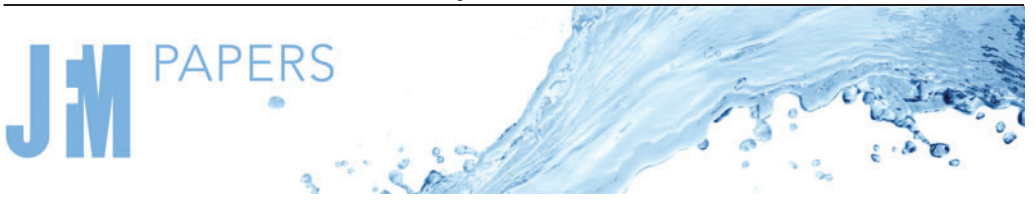

Binary collision dynamics of equal-sized nanodroplets

Yi-Feng Wang[1,2], Yi-Bo Wang[1,2], Zhi-Hui Cai[1,2], Qiang Ma[1,2], Yan-Ru Yang[1,2], Shao-Fei Zheng[1,2,†], Duu-Jong Lee[3,4] and Xiao-Dong Wang[1,2,†]

[1]State Key Laboratory of Alternate Electrical Power System withd Renewable Energy Sources, North China Electric Power University, Beijing 102206, PR China

[2]Research Center of Engineering Thermophysics, North China Electric Power University, Beijing 102206, PR China

[3]Department of Mechanical Engineering, City University of Hong Kong, Kowloon Tong 999077, Hong Kong

[4]Department of Chemical Engineering & Materials Science, Yuan Ze University, Chung-Li 32003, Taiwan

(Received 3 January 2023; revised 8 December 2023; accepted 10 December 2023)

Binary nanodroplet collisions have received increasing attention, whilst the identification of collision outcomes and the viscous dissipation mechanism have remained poorly understood. Using molecular dynamics simulations, this study investigates binary nanodroplet collisions over wide ranges of Weber number (*We*), Ohnesorge number (*Oh*) and off-centre distances. Coalescence, stretching separation and shattering are identified; however, bouncing, reflexive separation and rotational separation reported for millimetre-sized collisions are not observed, which is attributed to the enhanced viscous effect caused by the 'natural' high-viscosity characteristics of nanodroplets. Intriguingly, as an intermediate outcome, holes form in retracting films at relatively high *We*, arising from the vibration and thermal fluctuation of the films. Due to the combined effects of inertial, capillary and viscous forces, binary nanodroplet collisions fall into the cross-over regime, so estimating viscous dissipation becomes extremely important for distinguishing outcome boundaries. Based on the criterion that stretching separation is triggered only when the residual off-centre kinetic energy exceeds the surface energy required for separation, the boundary equation between coalescence and stretching separation is established. Here, viscous dissipation is calculated by the extracted flow feature from simulations, showing that the ratio of viscous dissipation to the initial kinetic energy depends only on *Oh*, not on *We*. Because of complex viscous dissipation mechanisms, the same boundary equation in the cross-over regime has also not been satisfactorily revealed for macroscale collisions. Therefore, the proposed equation is tested for wide data sources from both macroscale and nanoscale collisions, and satisfying agreement is achieved, demonstrating the universality of the equation.

† Email addresses for correspondence: shaofeizheng56@gmail.com, wangxd99@gmail.com

Key words: drops

1. Introduction

Binary droplet collisions are frequently encountered in natural and industrial processes, for example, droplets colliding in the air or in internal combustion engines (Faeth 1977). In the last three decades, binary droplet collision dynamics has been investigated experimentally (Jiang, Umemura & Law 1992; Qian & Law 1997; Bach, Koch & Gopinath 2004; Huang, Pan & Josserand 2019; Pan *et al.* 2019), numerically (Pan *et al.* 2019; Chaitanya, Sahu & Biswas 2021) and theoretically (Al-Dirawi *et al.* 2021). Particularly, the investigation of outcome regimes is emphasised owing to their practical significance. The binary droplet collision is controlled by the competition of inertial, capillary and viscous forces, the off-centre distance (χ) between two droplet centres, and gas environments. Therefore, Weber number ($We = \rho D_0 V_0^2/\gamma$), representing the ratio of inertial to capillary forces, Ohnesorge number ($Oh = \mu/(\rho D_0 \gamma)^{1/2}$), standing for the ratio of viscous to inertial-capillary forces, and the normalised off-centre distance ($B = \chi/D_0$) are used to describe the collision dynamics, where ρ is the density of the liquid, D_0 is the initial diameter of droplets, γ is the surface tension, μ is the viscosity of the liquid and V_0 is the impact velocity of droplets, i.e. half of the relative velocity between droplets. However, the construction of a three-dimensional phase diagram is extremely complex, so a *We*–*B* phase diagram is frequently drawn to present outcome regimes in a certain gas environment, taking *Oh* as a parametric variable.

As shown in figure 1, the pioneering study on outcome regimes by Qian & Law (1997) and the current literature (Pan, Chou & Tseng 2009; Pan *et al.* 2019) reported a total of six outcomes, including coalescence (CO), bouncing (BO), reflexive separation (RES), stretching separation (SS), rotational separation (ROS) and shattering (SH). In a low-*We* range, Regimes CO and BO are present. Two droplets in Regime CO contact each other and merge into a larger one, whereas those in Regime BO do not touch each other but instead bounce off the compressed gas cushion between them. The separation regimes (RES, SS and ROS) take place in a high-*We* range but in different *B* ranges. Regime RES occurs in a low-*B* range and represents that a merged droplet after significant spreading can be transformed back into two individual droplets moving away from each other; however, Regime SS takes place in a high-*B* range, which is indicative of significant stretching between the two droplets and then fast separation. Regime ROS, recently proposed by Pan *et al*. (2019), is similar to Regime SS but in a lower *B* range. In addition, the merged droplet in Regime ROS has significant rotation instead of fast separation in Regime SS. When *We* is extremely large, Regime SH appears, and the merged droplet breaks into many small daughter droplets.

When comparing *We*–*B* phase diagrams with different *Oh* and gas environments, several intriguing phenomena are found. First, with decreasing gas pressure (p), the gas cushion becomes difficult to form so that two droplets prefer to be in direct contact with each other, and the region of Regime BO is reduced (Qian & Law 1997). Second, increasing *Oh* impedes Regimes ROS and RES; therefore, the boundaries between these separation regimes and coalescence regime shift towards higher Weber numbers in *We*–*B* phase diagrams (Sommerfeld & Kuschel 2016; Pan *et al.* 2019). This is attributed to the fact that a strong viscous effect can lead to remarkable viscous dissipation, impeding the transition from coalescence to these separations. Third, the boundary between Regimes CO and SS also shows the same feature in most *Oh* ranges; however, intriguingly, in a special *Oh* range ($0.02 < Oh < 0.14$), this boundary collapses into a single curve, showing an inertial

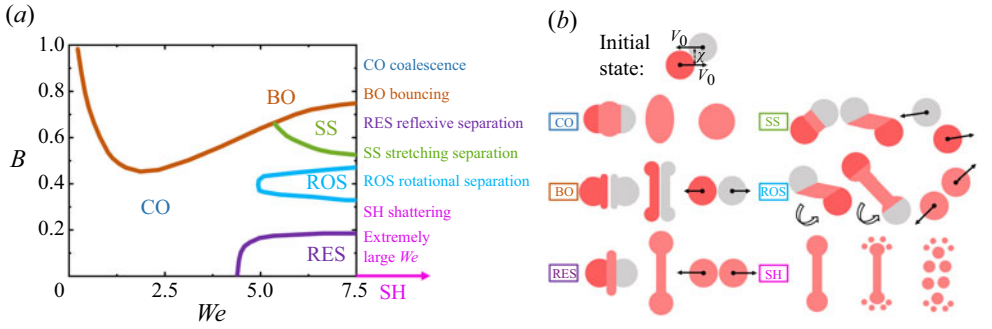

Figure 1. (*a*) A phase diagram of binary droplet collisions ($Oh = 0.0044$ and $D_0 = 0.6$ mm) in an atmospheric environment (Pan *et al.* 2019). (*b*) Schematics of outcomes, including coalescence (CO), bouncing (BO), reflexive separation (RES), stretching separation (SS), rotational separation (ROS) and shattering (SH). The Weber numbers in the original figure of Pan *et al.* (2019) are four times the Weber numbers in panel (*a*) because the relative velocity, $2V_0$, between two droplets is used by Pan *et al.* (2019) for calculating Weber numbers, whereas the velocity, V_0, of one droplet is considered in this work.

boundary (Al-Dirawi *et al.* 2021). Moreover, in this *Oh* range, the maximum stretching factor (l_{max}) in Regime CO is not sensitive to *Oh* as well, indicating inertial behaviours (Al-Dirawi *et al.* 2021). Because of the inertial boundary and the inertial behaviours, the inertial regime (viscous force is ignorable compared with inertial and capillary forces) can be defined in this special *Oh* range from 0.02 to 0.14. Once *Oh* falls below or increases above this range, the boundary between Regimes CO and SS and behaviours in Regime CO become viscosity dependent, and they transition from the inertial regime to the cross-over regime (viscous force is no longer negligible).

Compared with collisions in the inertial regime ($0.02 < Oh < 0.14$), collisions in the cross-over regime ($Oh > 0.14$) are also practically required. In internal combustion engines, reducing droplet diameters can significantly enhance combustion efficiency. As the diameter of an alkane (hexadecane) droplet reduces to O(μm), its Ohnesorge number can be increased to approximately 0.26, showing that the collision of such droplets falls into the cross-over regime. Unfortunately, despite the progress in the inertial regime ($0.02 < Oh < 0.14$), the viscosity-dependent dynamics of collisions in the cross-over regime ($Oh > 0.14$) has not been explored in detail. Owing to the enhanced viscous effect in such a high-*Oh* range, Regimes RES and ROS are significantly impeded, while Regime SS remains (Sommerfeld & Kuschel 2016). Identifying the boundary between Regimes CO and SS becomes important for understanding outcome regimes. Nonetheless, since the separation dynamics is no longer inertial, the viscous dissipation mechanism is altered, rendering describing the boundary extremely challenging.

For understanding the viscous dissipation mechanism, modelling the maximum spreading factor (β_{max}) is in demand, where β_{max} is the same as l_{max} at $B = 0$. Previous studies frequently model β_{max} by establishing an energy conservation equation from the initial state to the maximum spreading state to describe the viscous dissipation mechanism during spreading. Because the droplet is spherical at the initial state with a velocity of V_0 and forms a cylinder-like shape at the maximum spreading state with no remaining kinetic energy, the kinetic and surface energy at these states can be easily calculated. However, the calculation of the viscous dissipation during spreading is an extremely challenging task because information on evolving shapes and flow fields within the spreading droplet is additionally required. Early studies note that viscous dissipation concentrates in a cylinder-like sub-region, located at the centre of merged droplets, with stagnation flow

inside it, whereas viscous dissipation is negligible near spreading rims (Jiang *et al*. 1992; Qian & Law 1997). On the basis of this point, Pan *et al*. (2009) assumed that the stagnation flow region has a diameter of $D_0/2$ and a thickness of h_{min}, and the internal velocity gradients can be calculated by $V_0/(h_{min}/2)$, where h_{min} represents the minimal thickness, i.e. the thickness of the merged droplet at the maximum spreading state. Their β_{max} model includes both *We* and *Re* (or $Oh = We^{1/2}/Re$), indicating that the model is applicable to the cross-over regime. This model only qualitatively catches the dependence of β_{max} on both *We* and *Oh*; however, it shows significant deviation from their experiment data at a larger *Oh*. In contrast, Wildeman *et al*. (2016) claimed that instead of concentrating in the centre part of merged droplets, velocity gradients principally occur near the entrance of spreading rims, yielding an intriguing energy conversion feature where the stable proportion of the initial kinetic energy converts to viscous dissipation during spreading. This viscous dissipation mechanism implies that all binary droplet collisions are viscosity-independent and hence fall into the inertial regime. Recent experiment studies (Planchette *et al.* 2017; Al-Dirawi *et al.* 2021) proved that the constant proportion of viscous dissipation occurs only in a special *Oh* range from 0.02 to 0.14, but the proportion increases with *Oh* when *Oh* exceeds 0.14, indicating the transition from the inertial regime to the cross-over regime. Nonetheless, the viscous dissipation in the cross-over regime was not theoretically estimated by them. Therefore, the viscous dissipation mechanism needs to be satisfactorily revealed in the cross-over regime.

Nanodroplet-based technologies are rising recently, such as nanoscale inkjet printing (Galliker *et al.* 2012), the preparation of high-entropy materials (Glasscott *et al.* 2019) and so forth. Especially in inkjet printing processes, the minimal diameter of droplets is already reduced to 60 nm with an extremely high impact velocity of 250 m s^{-1}, as reported by Galliker *et al*. (2012), which shows practical requirements for studying the dynamics of nanodroplets. Due to the occurrence of the scale effect, viscous force is enhanced at the nanoscale (Li, Zhang & Chen 2015; Li, Li & Chen 2017; Wang *et al*. 2020*a*,*b*; Xie *et al*. 2020; Wang *et al*. 2021*a*,*b*; Lv *et al*. 2022; Wang *et al*. 2022*a*,*b*). Even for the typical low-viscosity liquid, water, the Ohnesorge number of a 10 nm water nanodroplet can be larger than 0.14, implying that the collision of nanodroplets possibly falls into the cross-over regime. Recently, there have been studies on the binary nanodroplet collision, including outcome regimes and modelling β_{max}. Yin *et al*. (2021) investigated collisions of nanodroplets in a vacuum and found that Regimes BO, RES and ROS do not take place at the nanoscale in the tested *We* range from 0 to 300; as a result, Regimes CO, SS and SH occupy most regions of the phase diagram at the nanoscale. The strongly suppressed Regimes RES and ROS at the nanoscale accord with the macroscale feature in the cross-over regime and hence confirm the speculation that the binary nanodroplet collision falls into the cross-over regime. Zhang & Luo (2019) focused on head-on binary nanodroplet collisions in a wide range of pressures from 0 to 800 kPa and found a significant difference between macroscale and nanoscale droplets. At the macroscale, increasing p can enlarge the area of Regime BO in a phase diagram and even cause bouncing for head-on collisions. For instance, the bouncing for the head-on collision of binary tetradecane droplets can take place at $p = 100$ kPa (Qian & Law 1997). However, at the nanoscale, bouncing is not able to take place for head-on collisions unless the gas pressure is increased to 270 kPa (Zhang & Luo 2019). Subsequently, Zhang & Luo (2019) reported a new outcome regime at the nanoscale, i.e. a hole regime, which prefers to take place in a high-*We* range for head-on collisions. In addition, they established a model of β_{max} for head-on collisions in a vacuum, which shows relatively good agreement with their MD data in a low-*We* range; however, the model is found not to be able to describe

β_{max} in a high-p range because β_{max} is significantly reduced with increasing p at the nanoscale. Furthermore, Zhang *et al*. (2021) compared collisions of nanodroplets with diameters of 10, 50 and 100 nm, and reported that the hole regime takes place for 10 and 50 nm nanodroplets but vanishes for 100 nm nanodroplets. Instead of the hole regime, Regime RES is observed for 100 nm nanodroplets, indicating the scale-dependent hole regime.

Despite preliminary identification of outcome regimes, neither the regime boundaries nor the viscous dissipation mechanism during spreading is satisfactorily described at the nanoscale. Due to the naturally high *Oh* of nanodroplets, binary nanodroplet collisions principally fall into the cross-over regime, indicating further difficulty in solving these two issues. It should be emphasised that even at the macroscale, such key issues are not well revealed in the cross-over regime. As a result, investigating the regime boundaries and the viscous dissipation mechanism at the nanoscale is expected to not only fill the gap at the nanoscale, but also contribute to the understanding of the collision dynamics at the macroscale.

This study investigates binary collisions of nanodroplets that can be naturally considered high-viscosity droplets, aiming to reveal the boundaries of outcome regimes and the viscous dissipation mechanism in the cross-over regime. First, in a vacuum, binary collisions of nanodroplets with different diameters and wide *We* and *B* ranges are tested in a systematic and thorough way to identify outcome regimes. A scaling law is subsequently derived to describe the boundary between Regimes CO and SS by considering the balance between kinetic and surface energy, with its prefactor including the ratio (α) of the viscous dissipation during spreading to the initial kinetic energy. Second, also in the vacuum condition, the maximum spreading factor is modelled by establishing an energy conservation equation, in which an assumption of velocity gradients is proposed with the help of extracted velocity distributions in nanodroplets from MD simulations. Using the model of β_{max}, α is obtained. Here, it needs to be emphasised that the scaling law of stretching separation boundary and the model of β_{max} are expected to be valid for both nanodroplets and high-viscosity macroscale droplets. Third, the collision of nanodroplets is investigated at high gas pressures. In this part, Regime BO and the effect of gas pressure on β_{max} are explored.

2. Simulation method

MD simulations, which are implemented by the LAMMPS (large-scale atomic/molecular massively parallel simulation) package, are used to investigate the binary droplet collision dynamics at the nanoscale. Figure 2 shows the schematic of the simulation system with a dimension of $100 \times 100 \times 100$ nm^3, where periodic boundary conditions are applied in all three directions. The two equal-sized water nanodroplets are produced by face-centred cubic (fcc) crystals based on the corresponding density at 300 K. This work attempts to reveal the collision dynamics of nanodroplets with diameters ranging from several nanometres to hundreds of nanometres. To reduce the computational cost, the nanodroplets with relatively low diameters of 6($\pm$0.3), 8($\pm$0.3) and 10($\pm$0.4) nm are simulated, containing water molecule numbers of 3782, 8968 and 17 517, respectively. This treatment is valid because, throughout the nanoscale, nanodroplets should follow the same collision dynamics, provided that the dominant dimensionless number group (*We*, *Oh* and *B*) is the same. Here, the calculations of the dimensionless numbers (*We* and *Oh*) use the average values of the diameters (i.e. 6, 8 and 10 nm), and these three diameters create a range of *Oh* from 0.35 to 0.45.

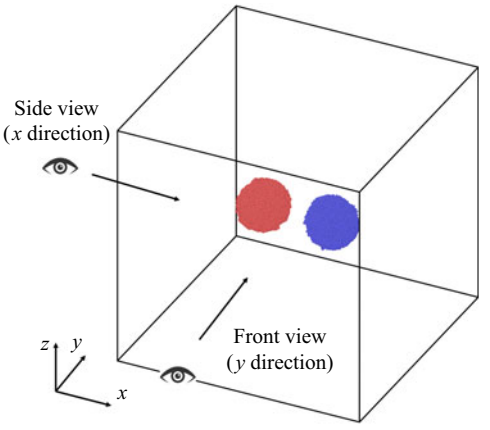

Figure 2. Schematic of the simulation system containing two nanodroplets, where two views for observing the dynamic behaviour of nanodroplets are shown.

MD simulations solve Newton's equations of motion to get the evolution of all particles in the simulation system, including the information of position, $\boldsymbol{r}_i = (x_i,\ y_i,\ z_i)$, and velocity, $\boldsymbol{V}_i = (V_{x,i},\ V_{y,i},\ V_{z,i})$, i.e.

$$m_i \frac{\mathrm{d}^2 \boldsymbol{r}_i}{\mathrm{d}t^2} = m_i \frac{\mathrm{d}\boldsymbol{V}_i}{\mathrm{d}t} = \boldsymbol{F}_i = \sum_{j \neq i} -\nabla U(r_{ij}), \tag{2.1}$$

where m_i is the mass of particle i, $\boldsymbol{F}_i$ is the force exerted on particle i by others, $U(r_{ij})$ is the potential function to describe the interaction between particles i and j, and r_{ij} is the distance between them.

Many water models have been developed to describe water within the framework of the MD simulation method. Owing to different assumptions of water structure and potential, the water described by these models has different physical properties from each other. Moreover, almost all current water models for MD simulations can only partially reproduce the key properties (ρ, γ and μ) (Molinero & Moore 2009). Therefore, the liquid described by each water model can be treated as an artificial liquid. However, fortunately, for the binary collision dynamics of equal-sized droplets at the nanoscale, when the values of the dimensionless parameter group (We, Oh and B) remain constant, the collision dynamics is uniquely determined, regardless of the choice of liquids. In other words, in MD simulations, the investigation of the collision dynamics is independent of the choice of potentials (see supplementary figure S1 available at https://doi.org/10.1017/jfm.2023.1069). Based on this point, the mW water model is chosen to describe the water because it is a coarse-grained model that can significantly reduce the computational cost. This water model is expressed as

$$U_{mW}(r_{ij}) = \sum_i \sum_{j>i} \varphi_1(r_{ij}) + \sum_i \sum_{j \neq i} \sum_{k>j} \varphi_2(r_{ij}, r_{ik}, \theta_{ijk}), \tag{2.2}$$

$$\varphi_1(r_{ij}) = A\varepsilon \left[B \left(\frac{\sigma}{r_{ij}} \right)^p - \left(\frac{\sigma}{r_{ij}} \right)^q \right] \exp\left(\frac{\sigma}{r_{ij} - a\sigma} \right), \tag{2.3}$$

$$\varphi_2(r_{ij}, r_{ik}, \theta_{ijk}) = \lambda_t \varepsilon [\cos\theta_{ijk} - \cos\theta^0]^2 \exp\left(\frac{\gamma\sigma}{r_{ij} - a\sigma} \right) \exp\left(\frac{\gamma\sigma}{r_{ik} - a\sigma} \right), \tag{2.4}$$

where $A = 7.049556277$, $B = 0.6022245584$, $p = 4$, $q = 0$, $\gamma = 1.2$, $a = 1.8$ and $\theta^0 = 109.47°$ are from the original Stillinger–Weber potential (Stillinger & Weber 1985), whereas the tetrahedral parameter λ_t (describing the strength of the tetrahedral interaction), the energy scale (ε) and the distance scale (σ) are tuned to $\lambda_t = 23.15$, $\varepsilon = 0.2684$ eV and $\sigma = 0.23925$ nm for producing the mW model (Molinero & Moore 2009). According to Molinero & Moore (2009) and Jacobson, Kirby & Molinero (2014), the properties of mW water are $\rho = 996$ kg m^{-3}, $\gamma = 66$ mN m^{-1} and $\mu = 0.2837$ mPa s. It should be noted that these parameters are all calculated from MD simulations based on the mW model. For example, considering a periodic simulation box with a slab of liquid inside it, as shown in figure S2, the surface tension can be calculated by $1/2L_N[\langle p_N\rangle - \langle p_T\rangle]$ (Kirkwood & Buff 1949), where L_N is the length of the simulation box in the direction normal to the slab of liquid, and $\langle p_N\rangle$ and $\langle p_T\rangle$ are the time-averaged components of the pressure tensors tangential (p_T) and normal (p_N) to the slab of liquid over an equilibrium simulation. It is worth noting that the choice of the mW model may lead to a problem of reproducing the saturated vapour pressure of water. The mW model is proposed by Molinero & Moore (2009) to describe the molecular interaction of water, by modifying the original Stillinger–Weber potential that is used to model the solid and liquid forms of silicon (Stillinger & Weber 1985). Silicon has an extremely low saturated vapour pressure; for example, its saturated vapour pressure is not larger than 15 Pa at a super-high temperature of 2102 K according to Stevanovic (1984); therefore, the mW water model significantly underestimated the saturated vapour pressure of water so that the gas space can be approximately treated as a vacuum at 300 K, as shown in figure S3(*a–c*). However, such an underestimation is proven not to affect the reliability of the mW water model for the prediction of nanodroplet collision dynamics (please see supplementary material, figure S3). In addition, as shown in figure S4, the change in the numbers of gas molecules during collisions are extracted for mW water, TIP3P water and LJ argon at $Oh = 0.49$ and $We = 25$, whose β_{max} have been proven the same (figure S1), indicating that MD simulations can capture the evaporation during collisions and such evaporation does not affect the collision dynamics.

At the macroscale, the choice of gas has been proven to affect the collision process due to the different gas molecular weight and viscosity; however, Regime BO can always take place once the gas pressure is large enough, no matter the kind of gas (Qian & Law 1997). In this work, the most focused issue in a gas environment is whether Regime BO can still exist at the nanoscale instead of detailed effect on collision dynamics, so only the gas pressure is concerned. Because argon (Ar) with a simple structure can result in high computational efficiency and is gaseous at 300 K, it is chosen to fill the simulation box for creating gas pressures. The interactions of Ar-water and Ar–Ar are both described by the 12-6 Lennard-Jones potential, expressed as

$$U_{LJ}(r_{ij}) = 4\varepsilon\left[\left(\frac{\sigma}{r_{ij}}\right)^{12} - \left(\frac{\sigma}{r_{ij}}\right)^{6}\right], \quad r_{ij} < r_{cut}, \tag{2.5}$$

where r_{cut} is the cut-off distance. The parameters for Ar–water and Ar–Ar interactions are $\varepsilon_{\mathrm{Ar-water}} = 0.0085$ eV, $\sigma_{\mathrm{Ar-water}} = 3.286$ Å, $\varepsilon_{\mathrm{Ar–Ar}} = 0.0103$ eV, and $\sigma_{\mathrm{Ar–Ar}} = 3.405$ Å, respectively, where the parameters for Ar–Ar interactions are from Yaguchi, Yano & Fujikawa (2010). For these interactions, r_{cut} is long enough to be set to 1 nm, as shown in figure S5. To test the effect of ambient gas at high pressures, the droplets are set far away from each other before collisions and the simulation system is filled with Ar atoms to create gas pressures of 120 and 450 kPa.

Each simulation includes three processes with a time step of 2 fs. The first process is an equilibrium process, conducted in the NVT ensemble (canonical ensemble) with a constant temperature of 300 K by the Nose–Hoover thermostat. In this process, two nanodroplets are fixed at a certain distance away from each other. After the simulation is implemented for 2 ns, the system achieves thermodynamic equilibrium and the equilibrium process ends. The second process is an approach process running in the NVE ensemble (micro-canonical ensemble), in which the two nanodroplets move close to each other with a given velocity. Once the two nanodroplets start to touch each other, the second process ends. The third process is a collision process (i.e. an outcome process), and many outcomes are possibly observed, depending on the collision condition, such as coalescence, separation and so forth. According to our tests, the formation of outcomes (i.e. the maximum stretching length does not change for coalescence, separation takes place for stretching separation and generated daughter droplets retract to spheres for shattering) are mostly within 500 ps; therefore, the collision process for all cases is implemented for 1 ns that is long enough to observe the whole collision process. The calculations for the cases of 6, 8 and 10 nm nanodroplets without additional gas molecules will require approximately 5, 10 and 16 h, respectively, on four threads on Intel Xeon E5-2697 v4 processors. The position and velocity of each water molecule are recorded every 1 ps for further analysis. For ensuring reliable statistics, we repeated the simulations of collisions of two 10 nm nanodroplets at low, medium and high Weber numbers (i.e. $We = 6$, 24 and 74) five times and recorded β_{max}, as shown in Table S1. The maximum relative deviation from the mean value of β_{max} at each Weber number does not exceed 1.5 %, showing the reliable statistics of the simulations.

3. Results and discussion

3.1. *Outcome regimes of collisions in a vacuum*

3.1.1. *Effects of We and B*

In this section, the outcome regimes of binary droplet collisions in a vacuum are discussed. At the macroscale, a total of six outcomes are reported, as shown in figure 1. However, there are only three outcomes for binary nanodroplet collisions, including CO, SS and SH, as shown in figure 3. As expected, due to the vacuum condition and the high-*Oh* effect, Regimes BO, RES and ROS are not found in the tested *We* range from 1 to 110 at the nanoscale. Here, instead of considering the formation of holes as a final outcome as done by the previous studies (Zhang & Luo 2019), the formation of holes is regarded as an intermediate outcome in this work, i.e. each final outcome can be further divided into two branches by whether holes form during collisions. As a result, the final outcomes with holes are further marked by an additional red circle, as shown in figure 3. For example, the outcome of coalescence with holes is marked by a blue square (representing coalescence) with an additional red circle (standing for a hole). Each outcome will be discussed in detail with the help of its typical snapshots, as shown in figures 4 and 5. The discussion of the outcome regimes is divided into two groups: (i) a low-*B* range ($B < 0.2$) and (ii) a high-*B* range ($B \geq 0.2$).

(i) Low-*B* range ($B < 0.2$)

In the low-*B* range, a binary nanodroplet collision is more like a head-on collision. Figure 3 shows that as *We* increases, nanodroplets sequentially undergo Regimes CO and SH, with holes forming in a high-*We* range. At a relatively low Weber number of 24, the collision is in Regime CO, as shown in figure 4(*a*). The two nanodroplets first merge into

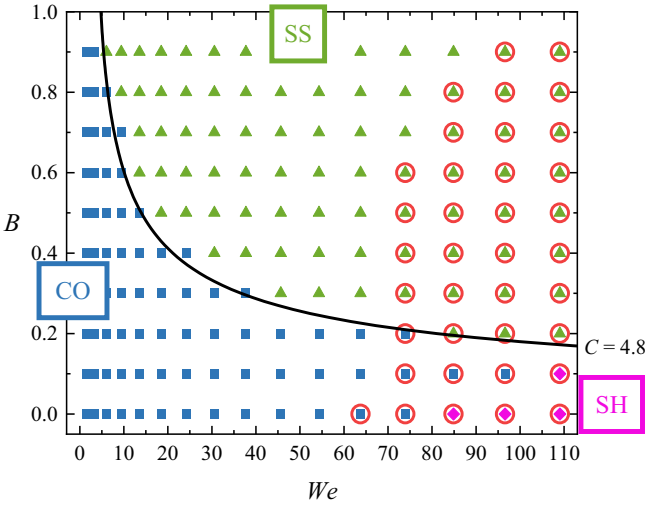

Figure 3. Phase diagram of binary nanodroplet collisions with $Oh = 0.35$, including coalescence (CO), stretching separation (SS) and shattering (SH). It should be emphasised that the hole is an intermediate outcome marked by a red circle based on the final outcomes (CO, SS and SH).

a single droplet and spread to the maximum spreading diameter without residual kinetic energy ($t = 35$ ps); subsequently, by releasing the surface energy stored in the deformation at the maximum spreading state, the merged droplet retracts ($t = 75$ ps) and reflexively stretches to the maximum extent against the collision direction ($t = 120$ ps). The reflexive separation does not take place, and the merged droplet eventually equilibrates into a sphere under the action of surface tension ($t = 200$ ps). At the macroscale, at a low Weber number of 8 (Qian & Law 1997), the merged droplet can stretch and form a dumbbell-like shape, i.e. the critical shape to generate Regime RES. However, at the nanoscale, although the Weber number is increased to a larger value of 54, the dumbbell-like shape is still not observed, as shown in figure 4(*b*). Eventually, no reflexive separation is found in all the present simulation cases, as shown in figure 3. This may be ascribed to the fact that the enhanced viscous force significantly increases the viscous dissipation during spreading. As *We* continues to increase to 74, the two droplets still coalesce into a merged droplet ($t = 10$ ps), but holes are generated in the retraction process ($t = 60$ ps), as shown in figure 4(*c*). Subsequently, the holes are refilled at $t = 140$ ps, and the following dynamic behaviours of the merged nanodroplet are identical to those in Regime CO without holes.

Here, it should be noted that no holes can be observed during binary droplet collisions at the macroscale (Pan *et al*. 2009; Liu & Bothe 2016). Using MD simulations, Zhang *et al*. (2021) have also found that the hole outcome will no longer be observed as the diameter of droplets increases to 100 nm. Therefore, the generation of holes for binary droplet collisions is limited to small scales. At the nanoscale, the outcome of holes is reported not only in head-on collisions (Zhang & Luo 2019; Zhang *et al*. 2021) but also in another similar process, i.e. the impact of a nanodroplet on a smooth solid surface (Li *et al*. 2017; Wang *et al*. 2021*b*). Li *et al*. (2017) and Wang *et al*. (2021*b*) interpreted that holes at the nanoscale are induced by the violent vibration of liquid films at relatively high Weber numbers. However, this interpretation is possibly doubtful because the centre of the liquid film is expected to experience the most violent vibration, but holes disorderly form in the interior of the film instead of at the centre, as shown in figure 4(*c*) and snapshots in the previous studies (Li *et al*. 2017; Wang *et al*. 2021*b*).

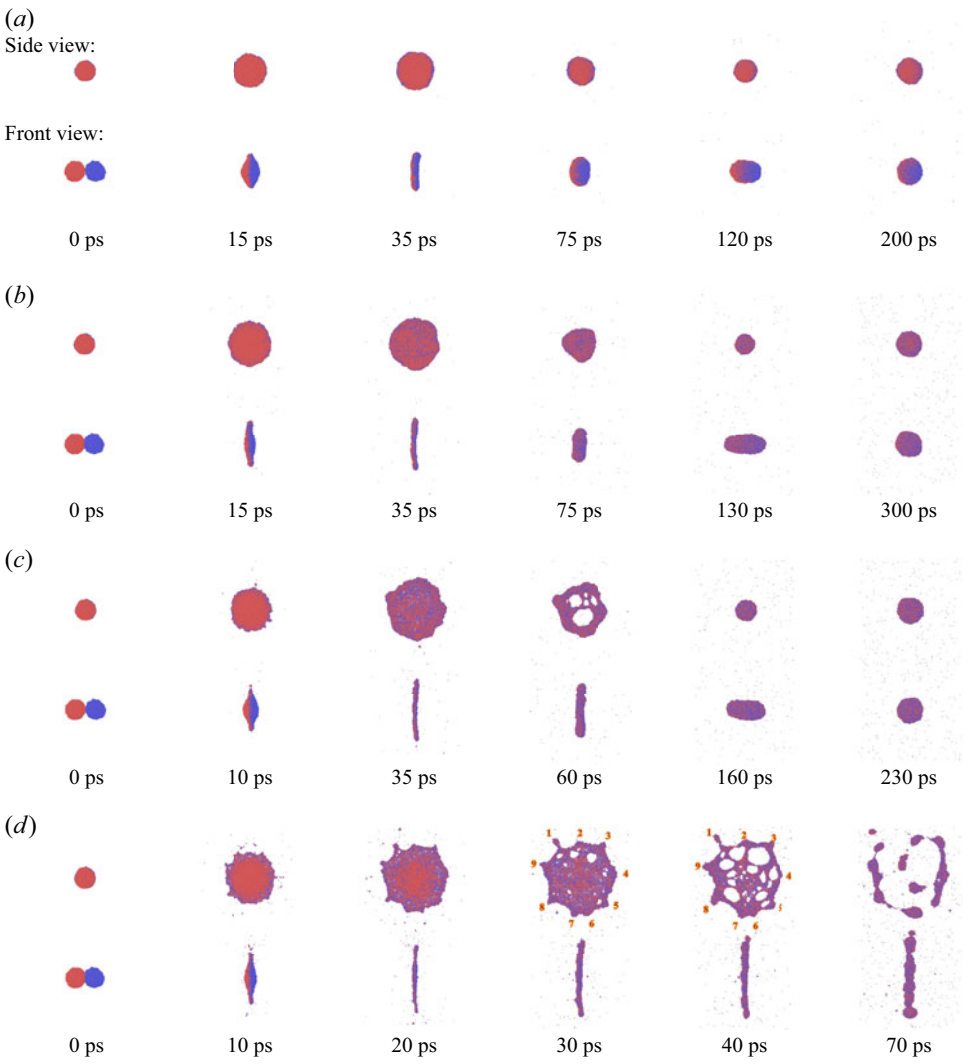

Figure 4. Snapshots of head-on binary nanodroplet collisions at $We = (a)$ 24, (b) 54, (c) 74 and (d) 109. The numbers shown in panel (d) at $t = 30$ and 40 ps highlight the positions of jetted fingers. It is worth noting that when the thickness of the peripheric rim is larger than the one at the centre of liquid films, only the outline of the rim can be seen in the front view. To show the relative thickness between the rim and the centre of liquid films, supplemented sliced snapshots near the beginning of forming holes for panel (c,d) are shown in figure S6(e,f).

Another possible mechanism, thermal fluctuations, is proposed here to interpret the generation of holes. Moseler & Landman (2000) investigated liquid jets at the nanoscale using MD simulations and claimed that the instability is induced by thermal fluctuations. To prove this, they added a stochastic stress tensor to the standard NS equations, and a stochastic lubrication equation (SLE) was derived to simulate the liquid jets at the nanoscale. Good agreement between the MD and SLE results is found. Subsequently, Hennequin *et al*. (2006) experimentally attested that thermal fluctuations can play an important role in liquid instability at very small scales and proved that the extended NS equations are able to describe the instability of liquid when thermal fluctuations are dominant. Based on these studies, it can be concluded that thermal fluctuations are

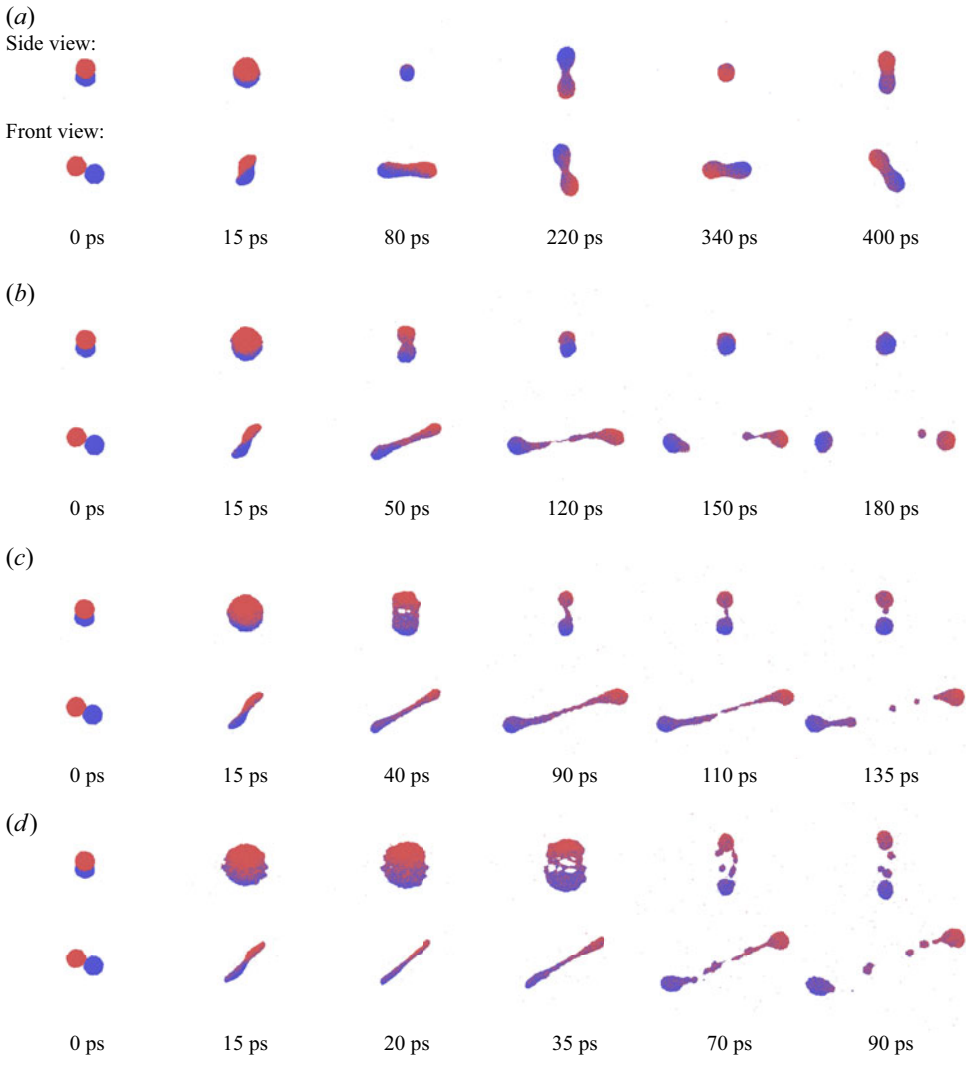

Figure 5. Snapshots of off-centre binary nanodroplet collisions at $We =$ (*a*) 24, (*b*) 54, (*c*) 74 and (*d*) 109.

important for liquid instability at the nanoscale, and MD simulations can accurately simulate the effect of thermal fluctuations. Recently, Zhang, Sprittles & Lockerby (2019) investigated the instability of liquid films with thicknesses of 1.18, 1.57 and 1.96 nm. Their MD results show that the films have unstable surfaces and spontaneously break up at their internal parts due to the action of thermal fluctuations. Based on this result, as expected, the liquid film at the maximum spreading state in figure 4(*c*), which has a thickness of less than 2 nm, does have unstable surfaces due to thermal fluctuations. As a result, the thermal fluctuations and the strong vibration at relatively large Weber numbers jointly induce the formation of holes. This insight not only interprets why holes disorderly form in the interior part of liquid films, but also answers why no holes generate when the diameter of nanodroplets increases to 100 nm (Zhang *et al.* 2021).

After the formation of holes, hole-refilling is observed, as shown in figure 4(*c*). Here, its mechanism is discussed, with the help of a series of detailed snapshots. As shown in figure S6(*a*), holes are formed in the retraction stage at 50 ps. With the action of surface

tension, the holes rapidly expand and merge into a large one from 50 to 69 ps. Meanwhile, the outer rim has started to retract at considerable speed. At $t = 69$ ps, the merged hole stops expanding because it comes up against the retracting rim. After that, the merged hole begins to retract along with the retracting rim from 69 to 83 ps, and eventually, the hole is completely refilled at $t = 85$ ps. Therefore, the hole-refilling can be attributed to the intensely retracting rim. In addition, the hole-refilling process is also observed by other potential models (an LJ liquid argon, the TIP3P water and the SPCE water), as shown in figure S6(*b–d*). As a result, the hole-refilling does not rely on the choice of potential models and hence is physical.

At an extremely large *We* of 109, the collision enters Regime SH. Figure 4(*d*) shows that the merged droplet has an irregular and unstable periphery during spreading ($t = 10$ and 17 ps) with holes appearing and growing in its internal part ($t = 36$ and 40 ps). Instead of the formed rim when holes emerge at $We = 74$, as shown in figure S6(*e*), such an irregular and unstable periphery at $We = 109$ inhibits the formation of retracting rim, as shown in figure S6(*f*); as a result, the expending of holes cannot be stopped and eventually the merged droplet shatters ($t = 70$ ps). Pan *et al*. (2009) who studied macroscale binary droplet collisions in Regime SH have pointed out that the irregular and unstable periphery is attributed to Rayleigh–Taylor instability. The difference in the unstable periphery between the macroscale and the nanoscale lies in that the formed fingers at the macroscale are lathy, but those at the nanoscale are stubby. In addition, Wang *et al*. (2021*b*) also reported that the splash of a nanodroplet impacting a solid surface is due to Rayleigh–Taylor instability. According to these studies, the shattering in binary nanodroplet collisions is expected to be caused by the Rayleigh–Taylor instability as well. Inspired by Wang *et al*. (2021*b*), the Rayleigh–Taylor instability during the fast spreading of thin films is tested by comparing the MD results of the interfacial waves at the periphery of nanodroplets with the theoretical results of the Rayleigh–Taylor instability. According to the Rayleigh–Taylor instability theory developed by Allen (1975), the finger number can be calculated by $N = [k\rho/(12\gamma)]^{1/2} D_0 \beta_{max}$, where k is the deceleration rate calculated by V_0^2/D_0. Using $\beta_{max} \approx 3$ extracted from the snapshots at 30 and 40 ps in figure 4(*d*), N is theoretically obtained as 9, which shows good agreement with the MD result at 30 and 40 ps in figure 4(*d*), and therefore indicates that the present data are consistent with the Rayleigh–Taylor instability theory. Further tests for nanodroplets with diameters of 6 and 8 nm are also implemented to prove this consistency, as shown in figure S7.

(ii) High-B range ($B \geq 0.2$)

In the high-B range, the off-centre effect becomes significant. As shown in figure 5(*a*), at a low *We* of 24, the higher B reduces the head-on area between the two droplets and enhances the stretching behaviour ($t = 15$ ps). Subsequently, the merged droplet is continuously stretched by the residual initial kinetic energy, with the central liquid bridge becoming thinner ($t = 80$ ps), accompanied by rotational motion. After the centre of the droplet reaches the thinnest thickness ($t = 220$ ps), the liquid bridge gradually grows ($t = 340$ ps) until its thickness increases to the ends' thickness of the merged droplet ($t = 400$ ps), showing Regime CO. When *We* increases to 54, larger off-centre kinetic energy is present, leading to the transition from Regime CO to SS. As shown in figure 5(*b*), the early collision process in Regime SS, including the stretching ($t = 15$ ps) and the formation of a thin liquid bridge ($t = 50$ ps), does not show a significant difference from the one in Regime CO shown in figure 5(*a*), whereas in the later process, the liquid bridge does not stop becoming further thinner ($t = 120$ ps) and finally breaks up ($t = 150$ ps), generating separated daughter droplets ($t = 180$ ps). At a larger *We* of 74,

holes generate at the centre of the merged droplet during stretching, as shown in figure 5(*c*). Furthermore, the deformation of merged droplets is enhanced and the number of holes is raised with a further increase in *We*, as shown in figure 5(*d*).

3.1.2. *Modelling the boundary of the stretching separation regime*

Regimes CO and SS occupy most regions of the phase diagram at the nanoscale, as shown in figure 3, and thereby, identifying the boundary between them is important for understanding the outcome regimes. In an early study, Jiang *et al*. (1992) assumed the separation process as two short cylinders grazing and finally departing from each other and correspondingly established a model for describing the boundary, expressed as $B = c_1 We^{-1/2}[1 + c_2 \mu\gamma^{-3/2}\rho^{1/2}D_0^{1/2}]$, where c_1 and c_2 are both fitting parameters. The model can satisfactorily fit the boundary in wide collision conditions, whereas these fitting parameters vary with the properties of liquid, indicating a lack of universality. This may arise from the fact that the actual shape of stretching droplets greatly deviates from the excessively constrained assumption of the cylinder shape. More recently, Al-Dirawi *et al*. (2021) experimentally found that the stretching separation of merged droplets follows a universal critical maximum stretching factor ($l_{max,cr}$) of 3.35, above which the stretching separation can take place. They, therefore, established a model of l_{max} to predict the boundary. Here, l_{max} is considered to be contributed by head-on and off-centre parts when $B > 0.2$, expressed as $l_{max} = \beta_{max} + s(B - 0.2)$, where s is an off-centre fitting function as $s = 0.049We + 2.58$. The model of β_{max} is built based on the assumption of the constant proportion (α) of the viscous dissipation during spreading to the initial kinetic energy at each *Oh*, and s is obtained by data fitting as a *We*-dependent function. Substituting $l_{max,cr} = 3.35$ in the model of l_{max}, the equation of the stretching separation boundary is obtained. This model can accurately predict the boundary between Regimes CO and SS in both inertial and cross-over regimes. In the inertial regime, the boundary is independent of *Oh*, so the model with a constant value of $\alpha = 0.65$ can predict the boundary at different *Oh*; in the cross-over regime, because the boundary is dependent on *Oh*, the model can hold only when adjusting the value of α corresponding to *Oh*. However, the quantitative relationship between *Oh* and α has not been established. Furthermore, using the model of l_{max} to predict the boundary is complex because it requires the calculation of β_{max} from an implicit expression even if α is known. To simplify this, a simple scaling law of the stretching separation boundary is directly established in this work, in which α is incorporated into the prefactor of it. This scaling law is expected to be valid both in the inertial regime by a constant α and in the cross-over regime by an *Oh*-dependent α. Despite using *Oh*-dependent α in the cross-over regime, α is not extracted from experiments or simulations but is obtained by a model of β_{max} in which the viscous dissipation during spreading is directly calculated.

The scaling law of the stretching separation boundary is derived in this section. During off-centre collision, the off-centre kinetic energy, expressed as $\sim P_o \rho D_0^3 V_0^2$, principally contributes to the stretching of the merged droplet, where $P_o = -0.5B^3 + 1.5B$ is the off-centre factor (for detailed information, please see Appendix A). During stretching, the off-centre kinetic energy converts to viscous dissipation and surface energy stored in the deformation. Once the residual off-centre kinetic energy after overcoming viscous dissipation exceeds the surface energy required for triggering the stretching separation, the stretching separation could take place. Since B does not affect the viscous dissipation proportion during stretching (Al-Dirawi *et al*. 2021), the residual off-centre kinetic energy can be expressed as $\sim(1 - \alpha)P_o \rho D_0^3 V_0^2$. The required surface energy is difficult to directly express, but it should satisfy the following two restrictions. One is that it must increase

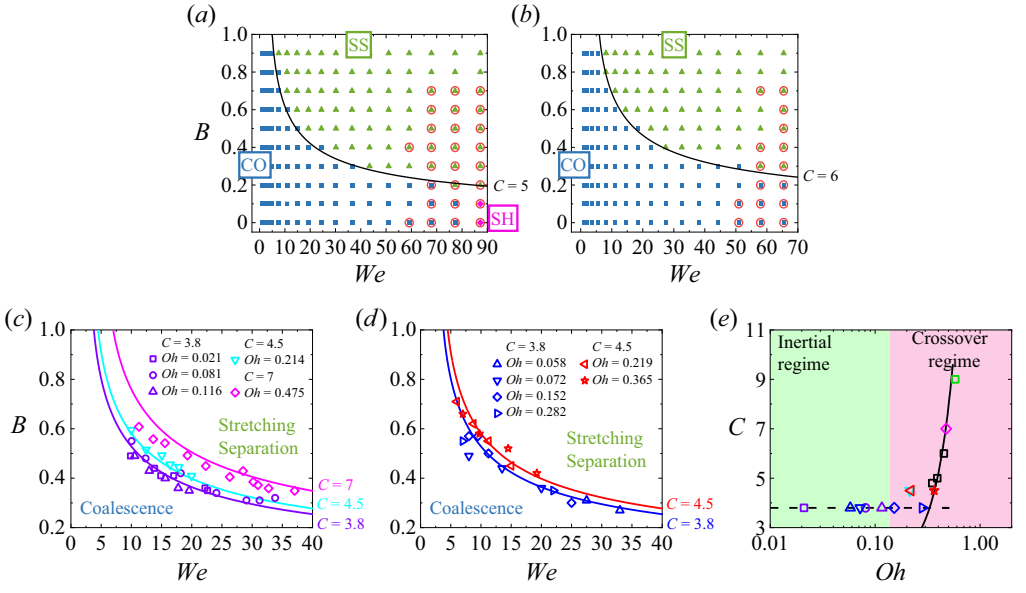

Figure 6. (*a*,*b*) Phase diagrams of binary nanodroplet collisions with $Oh = (a)$ 0.39 and (*b*) 0.45, where the solid line represents the proposed scaling law. (*c*,*d*) Boundary data of the stretching separation regime from (*c*) Al-Dirawi *et al.* (2021) and Sommerfeld & Pasternak (2019), and (*d*) Sommerfeld & Kuschel (2016). (*e*) Values of prefactor (C) obtained from figures 3, 6(*a–d*) and figure S8 at various Oh, where the values of C regressed from figures 3 and 6(*a*,*b*) are marked by black squares, and the value regressed from figure S8 is marked by a green square. Here, the dashed line represents a constant value of 3.8, and the solid line represents the predicted value by the scaling law of $C \sim (1-\alpha)^{-1}$, where the prefactor of this scaling is adopted as 1, and α is obtained by the model of β_{max}, i.e. (3.20).

when B decreases, which corresponds to the fact that reducing the off-centre effect can hinder the stretching separation behaviour. The other is that it must be infinite when $B = 0$, because stretching separation is impossible to take place in head-on collision processes, indicating that B must be larger than 0. These restrictions yield a simple scaling assumption for the required surface energy as $\sim \gamma D_0^2/B$. As a result, the scaling law for describing the stretching separation boundary is obtained as $\gamma D_0^2/B \sim (1-\alpha) P_o \rho D_0^3 V_0^2$. After rearranging this scaling law, the boundary equation of the transition from Regime CO to SS is

$$We = C(-0.5B^4 + 1.5B^2)^{-1}, \tag{3.1}$$

where C is the prefactor of the scaling law. This scaling law shows the energy balance between the off-centre kinetic energy and the required surface energy, with the viscous dissipation during stretching to be incorporated into its prefactor as $C \sim (1-\alpha)^{-1}$. When the viscous dissipation becomes larger (i.e. α and C are both larger), a smaller ratio of the initial kinetic energy can be used to promote the stretching for separation, leading to an increase in the requirement for the initial kinetic energy and also to the shifting of the critical Weber number towards high values. Using $C = 4.8$, (3.1) well fits the boundary between Regimes CO and SS, as shown in figure 3.

It should be emphasised that in the inertial regime, C is a constant due to constant α; however, in the cross-over regime, a large Oh increases viscous dissipation and hence leads to an increased C. To validate whether this scaling law covers the stretching separation boundary in both the inertial and cross-over regimes, another two phase diagrams for mW nanodroplets with $Oh = 0.39$ ($D_0 = 8$ nm) and 0.45 ($D_0 = 6$ nm) from this work are shown

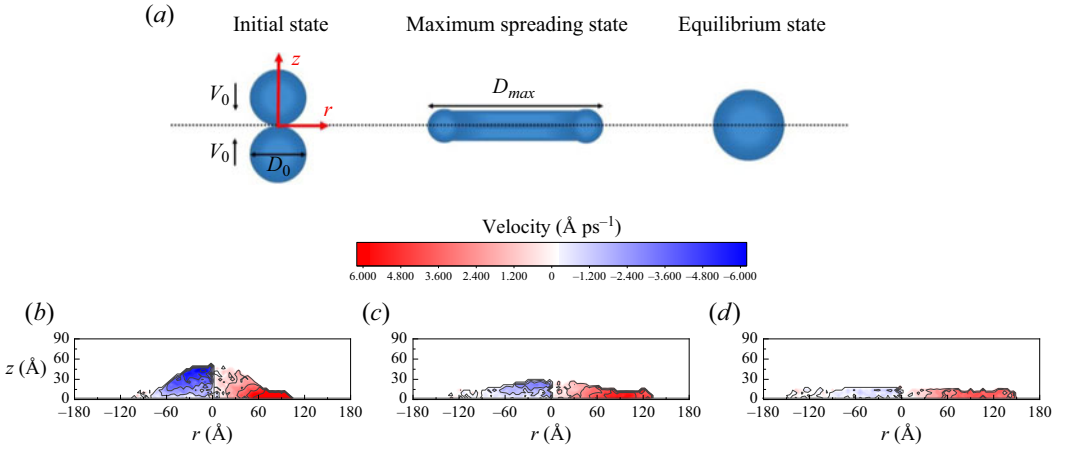

Figure 7. (*a*) Schematics of a head-on collision process and a symmetry plane, where, due to the symmetry, the collision can be considered as a nanodroplet impacting the imaginary symmetry plane, bringing the convenience of modelling β_{max}. (*b–d*) Velocity contours of head-on binary nanodroplet collisions at $We = 85$ at $t =$ (*a*) 8, (*b*) 13 and (*c*) 18 ps. The left side shows the velocity component in the impact direction, V_z, whereas the right side represents the velocity component in the spreading direction, V_r.

in figure 6(*a*,*b*), and an additional phase diagram for TIP4P nanodroplets with $Oh = 0.58$ from Yin *et al*. (2021) is shown in figure S8. Moreover, the experimental data on the stretching separation boundaries from the previous studies (Sommerfeld & Kuschel 2016; Sommerfeld & Pasternak 2019; Al-Dirawi *et al*. 2021) are also used to test the scaling law, as shown in figure 6(*c*,*d*). This scaling law can satisfactorily match the stretching separation boundaries at both the nanoscale and the macroscale. In a relatively low-*Oh* range, C is almost constant; however, in a relatively large-*Oh* range, C increases with *Oh*. To exhibit the relationship between C and *Oh*, the data of C versus *Oh* are drawn in figure 6(*e*). This figure shows that C remains constant at 3.8 in the inertial regime but increases with *Oh* in the cross-over regime. Nonetheless, it should be indicated that all values of C in figure 6(*a–d*) are obtained by regression. As a result, the model of β_{max} will be established in the next section to obtain α and hence C by $C \sim (1-\alpha)^{-1}$.

3.2. *Modelling β_{max} in a vacuum*

In this section, the head-on collision is discussed by modelling its feature parameter β_{max} for understanding the viscous dissipation mechanism and obtaining the ratio (α) of the viscous dissipation during spreading to the initial kinetic energy. The energy conservation equation of spreading is frequently established by considering kinetic energy (E_k), surface energy (E_s) and viscous dissipation (E_{dis}) from the initial state to the maximum spreading state, expressed as

$$E_{k,0} + E_{s,0} = E_{s,m} + E_{dis}, \tag{3.2}$$

where subscripts 0 and m denote the initial state and the maximum spreading state, respectively. Since the net flux of molecules across the symmetry plane can be safely regarded as null, the head-on binary droplet collision can be considered as a droplet impacting an imaginary symmetry plane. Therefore, only one of the two droplets is chosen as the subject in modelling, as shown in figure 7(*a*). This treatment brings convenience to the discussion of binary droplet collisions and the impacts of droplets on solid surfaces later.

The spherical shape of a nanodroplet before collision yields the expressions of $E_{k,0}$ and $E_{s,0}$ as

$$E_{k,0} = \tfrac{1}{12}\pi\rho D_0^3 V_0^2, \tag{3.3}$$

$$E_{s,0} = \gamma\pi D_0^2. \tag{3.4}$$

According to Li *et al*. (2017), $E_{s,m}$ for the nanodroplet at the maximum spreading state can be expressed as

$$E_{s,m} = \pi D_0^2\gamma\left(\frac{1}{3}\beta_{max}^2 + \frac{2}{3}\frac{1}{\beta_{max}}\right). \tag{3.5}$$

In a recent study (Al-Dirawi *et al*. 2021), it has been proven that α is constant in the inertial regime but increases with Oh in the cross-over regime. However, the quantitative relationship between α and Oh has not been satisfactorily established in the cross-over regime. Herein, the viscous dissipation is estimated by integration of the dissipation function, ϕ, as follows:

$$E_{dis} = \int_0^{t_s}\int_\Omega \phi\,\mathrm{d}\Omega\,\mathrm{d}t, \tag{3.6}$$

$$\phi = \mu\left(\frac{\partial v_i}{\partial x_j} + \frac{\partial v_j}{\partial x_i}\right)\frac{\partial v_i}{\partial x_j}. \tag{3.7}$$

Considering $V_\theta = 0$, (3.7) is simplified as

$$\phi = 2\mu\left[\left(\frac{\partial V_r}{\partial r}\right)^2 + \left(\frac{V_r}{r}\right)^2 + \left(\frac{\partial V_z}{\partial z}\right)^2 + \frac{1}{2}\left(\frac{\partial V_r}{\partial z} + \frac{\partial V_z}{\partial r}\right)^2\right], \tag{3.8}$$

where Ω is the volume of droplets, t_s is the spreading time, i.e. the time span for one of the two droplets from just touching the symmetry plane to attaining the maximum spreading state, V_r is the velocity component in the spreading direction (radial direction), V_z is the velocity component in the impact direction (axial direction), r is the coordinate of the spreading direction (radial direction) and z is the coordinate of the impact direction (axial direction). According to (3.8), the estimation of viscous dissipation requires information on velocity gradients; however, the velocity distribution feature within the nanodroplet in head-on collisions is still unknown. Zhang & Luo (2019) assumed that the velocity gradient of $\partial V_r/\partial z$ dominates the viscous dissipation during spreading, expressed as $\partial V_r/\partial z = (rV_0)/(RH)$, where R is the spreading radius and H is the height of droplets. Unfortunately, the model of β_{max} from Zhang & Luo (2019) based on this velocity assumption does not accurately fit MD data in a high-We range. This may be attributed to the fact that the no-slip condition usually takes place when liquid flows on a solid surface but significantly diverges from the free-spreading film in such head-on collisions. For precisely understanding velocity distributions within droplets, velocity contours are extracted from MD simulations by the following method. The simulation box is divided into many units with a dimension of $0.5 \times 0.5 \times 0.5$ nm^3, and then the velocity

components in spreading and impact directions in each unit are calculated by

$$\left.\begin{aligned} V_r &= \frac{\sum_{i=1}^{n} V_{r,i}}{n}, \\ V_z &= \frac{\sum_{i=1}^{n} V_{z,i}}{n}, \end{aligned}\right\} \tag{3.9}$$

where n is the number of molecules in a unit, and i is the ith molecule. The velocity contours of the merged nanodroplet during head-on collision at $We = 85$ are shown in figure 7(*b–d*). Each velocity component (V_r or V_z) shows a linear profile in its own direction (spreading or impact direction) but does not change in the other direction. In other words, $\partial V_r/\partial r$ (or $\partial V_z/\partial z$) is constant, but $\partial V_r/\partial z$ (or $\partial V_z/\partial r$) can be neglected. As a result, the velocity gradients of $\partial V_r/\partial r$ and $\partial V_z/\partial z$ play dominant roles in the viscous dissipation during spreading. Because of $V_{r|r=0} = 0$ and $V_{r|r=R} = V_s$, the distribution of V_r within nanodroplets can be expressed as

$$V_r = \frac{r}{R} V_s, \tag{3.10}$$

where V_s is the spreading velocity at the edge of the spreading film. According to the continuity equation,

$$\frac{\partial V_r}{\partial r} + \frac{\partial V_z}{\partial z} + \frac{V_r}{r} = 0, \tag{3.11}$$

the expression of V_z can be derived as

$$V_z = -\frac{2z}{R} V_s. \tag{3.12}$$

Unlike the assumption of velocity gradients, $\partial V_r/\partial z = (rV_0)/(RH)$, satisfying the no-slip condition (i.e. the shear flow feature), (3.10) and (3.12), following the free-slip condition (i.e. the extensional flow feature), can match better with the velocity contours shown in figure 7(*b–d*). Combining (3.8) with (3.10) and (3.12), the dissipation function is obtained,

$$\phi = \mu \frac{12}{R^2} V_s^2. \tag{3.13}$$

By integration with respect to space, (3.6) is transformed to

$$E_{dis} = \int_0^{t_s} [12\pi H \mu V_s^2] \, \mathrm{d}t. \tag{3.14}$$

According to the volume conservation, $\pi D_0^3/6 = \pi D(t)^2 H$, H could be replaced by $\beta(t)$, expressed as

$$H = \frac{2}{3} \frac{D_0}{\beta^2(t)}. \tag{3.15}$$

Substituting (3.15) in (3.14) yields

$$E_{dis} = \int_0^{t_s} \left[8\pi \mu D_0 V_s^2 \cdot \frac{1}{\beta^2(t)} \right] \mathrm{d}t. \tag{3.16}$$

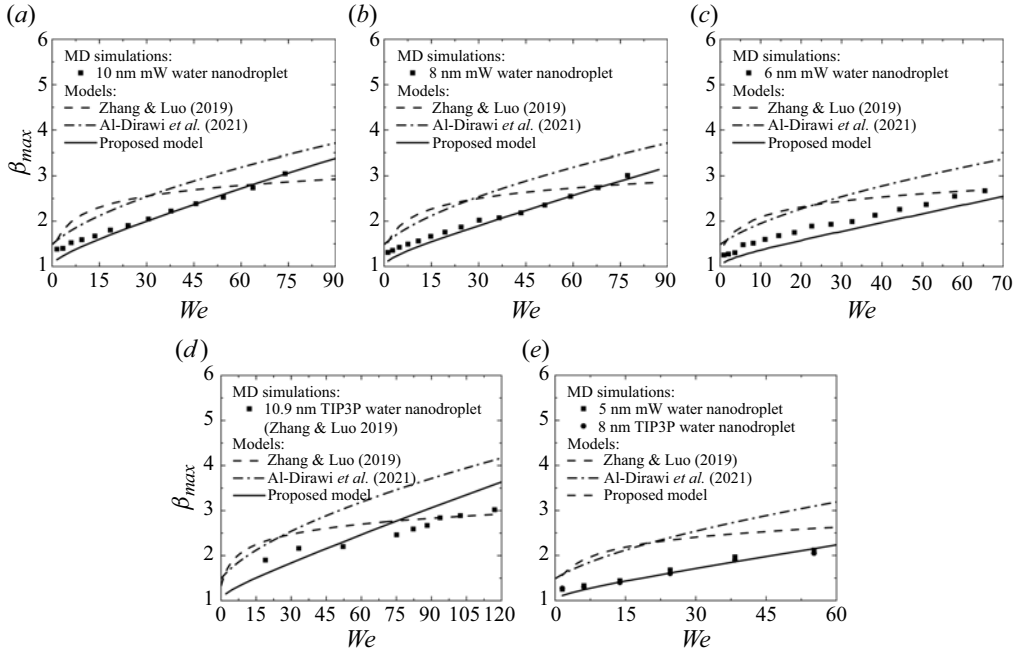

Figure 8. (*a–e*) Comparisons between theoretical results and MD data from both current and previous studies.

In addition, the differential of time, dt, can be replaced by the differential of the spreading factor, d$\beta(t)$, expressed as

$$\mathrm{d}\beta(t) = \frac{\mathrm{d}D(t)}{D_0} = 2\frac{\mathrm{d}R(t)}{D_0} = \frac{2V_s\,\mathrm{d}t}{D_0}. \tag{3.17}$$

Rearranging (3.17) leads to

$$\mathrm{d}t = \frac{D_0\,\mathrm{d}\beta(t)}{2V_s}. \tag{3.18}$$

Substituting (3.18) in (3.16), the expression of the viscous dissipation during spreading is finally obtained as

$$E_{dis} = 4\pi\mu D_0^2 V_s\left(1 - \frac{1}{\beta_{max}}\right). \tag{3.19}$$

Combining (3.2) with (3.3)–(3.5) and (3.19) leads to

$$\frac{1}{3}\beta_{max}^2 + \frac{2}{3}\frac{1}{\beta_{max}} - 1 = \frac{We}{12} - 4C_{vf}We^{1/2}Oh\left(1 - \frac{1}{\beta_{max}}\right), \tag{3.20}$$

where the velocity factor is $C_{vf} = V_s/V_0$. During spreading, the spreading velocity varies nonlinearly from a high value at the initial state to zero at the maximum spreading state. Here, an equivalent constant spreading velocity is adopted by data fitting. The spreading velocity (V_s) stems from the collision of droplets with the impact velocity (V_0), and therefore, it should increase with V_0. In addition, the internal extensional flow feature has been incorporated into this model, which relates the velocities in the impact and spreading directions. Based on these clues, it is expected that the spreading velocity scales as the

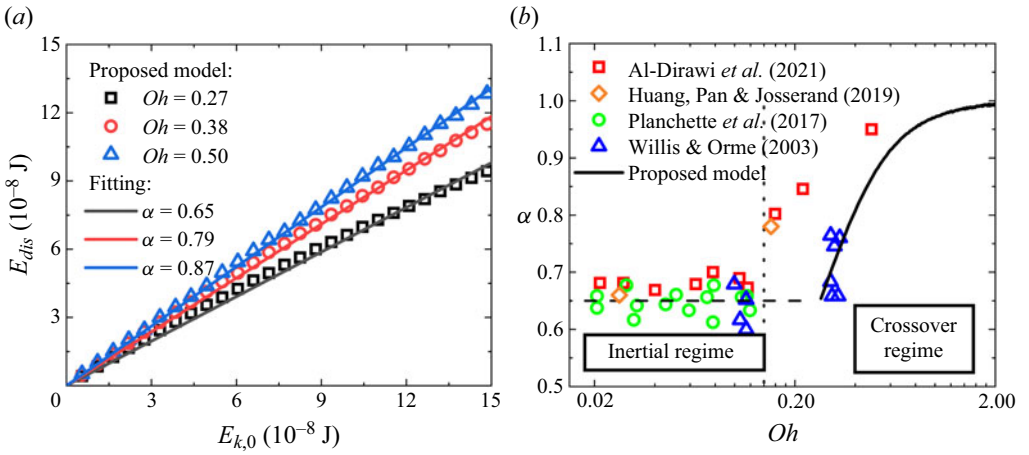

Figure 9. (*a*) Results of E_{dis} varying with $E_{k,0}$ at different Oh calculated by (3.20) and the corresponding linear fitting results. (*b*) Comparison between the predicted α by (3.20) and the measured α in previous experimental studies, where the dashed line presents a constant value of α in the inertial regime and the solid line shows the predicted α with the method shown in panel (*a*).

impact velocity (i.e. C_{vf} is a constant) in the cross-over regime. According to the data of β_{max} shown in figure 8(*a*), C_{vf} is taken as 0.48. For testing the universality of this fitting value, with $C_{vf} = 0.48$ as input, the proposed model of β_{max} is compared with the simulation data not only of mW water nanodroplets with diameters from 5 to 10 nm but also of TIP3P water nanodroplets with diameters of 8 and 10.9 nm (figure 8). To verify whether the molecular orientation and structure have special effects on β_{max}, figure 8(*e*) includes two series of data for both the mW water and the TIP3P water at the same Oh, where the mW water is a monatomic model and the TIP3P is a full-atom model. Good agreement is shown between the model and the MD simulation results for nanodroplets with various diameters and Weber numbers based on different water models, indicating the universality of the proposed model in the cross-over regime.

Using the proposed model of β_{max}, the value of E_{dis} is calculated at various We. As shown in figure 9(*a*), the predicted E_{dis} show linear dependence on $E_{k,0}$ at each Oh, indicating a constant value of $\alpha = E_{dis}/E_{k,0}$. This is consistent with the experimental observation in the previous studies (Planchette *et al.* 2017; Al-Dirawi *et al.* 2021). By fitting the slopes of E_{dis}–$E_{k,0}$ curves, α at different Oh is obtained. Figure 9(*b*) shows the data of α from previous studies (Willis & Orme 2003; Planchette *et al.* 2017; Huang, Pan & Josserand 2019; Al-Dirawi *et al.* 2021) in both the inertial and cross-over regimes. In the cross-over regime, the ratios (α) from Willis & Orme (2003) are lower than those from Huang, Pan & Josserand (2019) and Al-Dirawi *et al.* (2021). To the best of our knowledge, such differences have not been satisfactorily interpreted before. Two possible reasons are proposed here, i.e. the non-Newtonian effect and the gas pressure effect. However, Al-Dirawi *et al.* (2021) reported that HPMC and glycerol aqueous solutions show Newtonian behaviours in their study; in addition, the silicone oils used by Willis & Orme (2003) and Huang, Pan & Josserand (2019) can also safely be considered as Newtonian fluids, according to the study of Vázquez-Quesada *et al.* (2017). As a result, the non-Newtonian effect is excluded. Because the experiments of Willis & Orme (2003) were conducted in a vacuum, whereas those of the other studies were in an atmosphere, the lower α from Willis & Orme (2003) is more possibly ascribed to the gas pressure effect.

As expected, the proposed model of β_{max}, which is based on binary nanodroplet collisions in a vacuum, underpredicts the macroscale data of α in the atmosphere but shows good agreement with the macroscale data in the vacuum (Willis & Orme (2003)). Using α obtained by the model of β_{max} in the cross-over regime, the prefactor, $C \sim (1-\alpha)^{-1}$, of (3.1) is also determined, which shows good agreement with the data in the cross-over regime, as shown in figure 6(*e*). It should be emphasised that the value of C regressed from the phase diagram of Yin *et al*. (2021), who simulated the collisions by two TIP4P water nanodroplets, is also satisfactorily predicted by $C \sim (1-\alpha)^{-1}$, indicating that the collision dynamics obtained by different potential models of liquids is the same when the value of the dimensionless number group remains constant. This further proves that it is safe to investigate binary nanodroplet collisions by such a coarse-grained mW water model.

Although the established model of β_{max} successfully covers the viscous dissipation mechanism in the cross-over regime, the transition from the inertial to the cross-over regime has not been properly interpreted. Here, a possible reason for the transition is discussed based on the flow features in the inertial (Wildeman *et al*. 2016) and cross-over (this work) regimes. In the inertial regime, Wildeman *et al*. (2016) reported a viscosity-independent ratio of the viscous dissipation during spreading to the initial kinetic energy for head-on binary droplet collisions. They interpreted that this specific viscous dissipation mechanism corresponds to the flow feature that velocity gradients principally concentrate in the entrance region of the rim. However, as shown in figure 7(*b–d*), when collisions are in the cross-over regime, the velocity gradients are violent in entire droplets instead of only in the entrance region of the rim. Therefore, the transition mechanism from the inertial to the cross-over regime may result from the violent viscous dissipation extending from the entrance region of the rim to the entire droplet.

Since the impact of droplets on solid surfaces is similar to head-on binary droplet collisions, the current model of β_{max} in the cross-over regime is expected to be valid for impacting nanodroplets on solid surfaces as well. It is also desired to provide insights into the viscous dissipation mechanism during spreading on solid surfaces at the nanoscale because there is still a debate on the flow feature of nanoscale impact dynamics. Li *et al*. (2015) reported that the velocity gradient of $\partial V_z/\partial z = V_0/H$ dominates the viscous dissipation, whereas Li *et al*. (2017) claimed that $\partial V_r/\partial z = (rV_0)/(RH)$ contributes to the viscous dissipation. Nonetheless, both of them ignored some important velocity gradients. Wang *et al*. (2020*a*) proposed another velocity distribution for calculating the viscous dissipation, i.e. $V_r = V_s rz/(RH)$ and $V_z = -z^2 V_s/(RH)$, based on which no velocity gradient is ignored. These expressions satisfy the no-slip condition. However, the no-slip condition is significantly violated for impacting nanodroplets on solid surfaces (Koplik, Banavar & Willemsen 1988), implying that these expressions do not hold for the nanoscale impact on solid surfaces, and also showing the similarity between the impact on solid surfaces and head-on binary droplet collision at the nanoscale. Therefore, it is expected that the proposed model can also predict β_{max} for the impact of nanodroplets on solid surfaces. Nonetheless, the model can fit the data on a surface with $\theta = 180°$ only when the fitting parameter (C_{vf}) is modified to 0.85, as shown in figure 10(*a*). This may be attributed to the fact that solid surfaces render the viscous dissipation of impacting nanodroplets on them larger than that of binary droplet collisions. Wang *et al*. (2021*a*) reported that when $\theta > 73°$, the wettability has a relatively weak effect on the maximum spreading factor (β_{max}) for the impact of nanodroplets on solid surfaces. Therefore, the data of β_{max} on surfaces with θ from 73° to 148° are also used to further test the proposed model here. It is found that although the proposed model does not include the effect of contact angles, it still shows good agreement when $\theta \geq 125°$, as shown in figure 10(*b*), with a mean

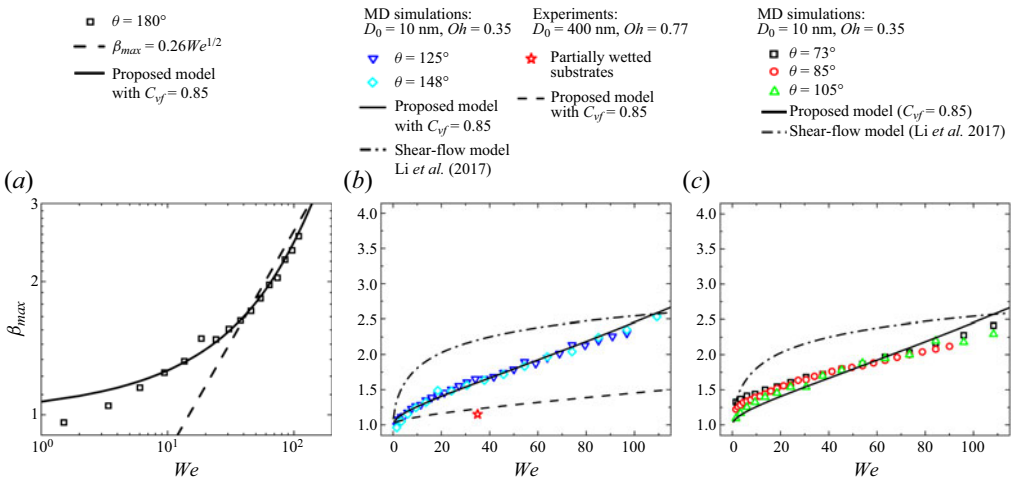

Figure 10. (*a*) Comparison among the MD data for impacting nanodroplets on solid surfaces with $\theta = 180°$, the scaling law of $\beta_{max} \sim We^{1/2}$ with a prefactor of 0.26 and the proposed model with $C_{vf} = 0.85$. (*b*,*c*) Comparison between the proposed model with $C_{vf} = 0.85$ and the MD data of β_{max} for nanodroplets on solid surfaces with (*b*) $\theta \geq 125°$ and (*c*) $\theta < 125°$. In addition, an experimental data point is also considered for comparison in panel (*b*).

relative error of 2.1 %. When $\theta < 125°$, the accuracy of the proposed model is reduced with underestimation in a low-*We* range and overestimation in a high-*We* range, as shown in figure 10(*c*). This can be attributed to the following two reasons. First, in a low-*We* range, stronger wettability can spontaneously increase β_{max}. Therefore, in the low-*We* range, the proposed model slightly underestimates the value of β_{max}. Second, stronger wettability may also reduce the slip effect, leading to increased viscous dissipation. This viscous dissipation is more significant at high *We*. Consequently, the proposed model overestimates β_{max} at high Weber numbers. The combination of these two reasons results in a steeper dependency of β_{max} on *We* than MD data when $\theta < 125°$. However, even if wettability comes into play, the prediction accuracy of our model remains acceptable, with the mean relative error only increasing to 6.4 %. To further demonstrate that the prediction accuracy is indeed improved by modifying the estimation of viscous dissipation in the proposed model, a recently developed nanoscale no-slip β_{max} model is also considered for comparison (Li *et al*. 2017). Comparing this no-slip model with the MD data reveals that the estimation of viscous dissipation has a dominant effect on both prediction accuracy and the dependence of β_{max} on *We*, as shown in figure 10(*b*,*c*). Therefore, our proposed model, using slip-based viscous dissipation estimation, not only improves prediction accuracy but also further elucidates the viscous dissipation mechanism behind nanoscale droplet impact on solid surfaces. In addition to the comparison with MD data, to further ensure the established model is useful in physical reality, the only data point on the maximum spreading factor of nanodroplets in a real inkjet printing process from Galliker *et al*. (2012) is also taken into consideration. As shown in figure 10(*b*), without any further modification, the established model can well fit the experimental value, proving the practical significance of the established model.

It should be emphasised that, intriguingly, in the wide *We* range from approximately 30 to 110, the data of β_{max} for nanodroplets coincide with the scaling law of $\beta_{max} \sim We^{1/2}$, as shown in figure 10(*a*); however, $\beta_{max} \sim We^{1/2}$ has never been observed in any experiments for millimetre-sized droplets impacting solid surfaces (Josserand & Thoroddsen 2016).

Here, the agreement between the prediction result of (3.20) and the scaling law of $\beta_{max} \sim We^{1/2}$ at the nanoscale indicates that the possible condition for the occurrence of the scaling of $\beta_{max} \sim We^{1/2}$ is the extensional flow feature. If that is not the case, the spreading droplet will have the shear flow feature, and the velocity gradient of $\partial V_r/\partial z(=(rV_0)/(RH))$ for the shear flow will make the expression of viscous dissipation include a term of β_{max}^5 (Li *et al*. 2017; Wang *et al.* 2020*a*), leading to remarkable viscous dissipation with increasing β_{max} and hence making the scaling law of $\beta_{max} \sim We^{1/2}$ impossible. This argument provides a possible reason why $\beta_{max} \sim We^{1/2}$ has never been observed for millimetre-sized impacting droplets on solid surfaces (Josserand & Thoroddsen 2016).

3.3. *Effect of ambient gas*

All discussion in §§ 3.1 and 3.2 is implemented in a vacuum condition by mW droplets, therefore under the dimensionless parameter group of *We*, *Oh* and *B*. However, the effect of ambient gas is also an important parameter affecting the collision dynamics of droplets. In previous macroscale studies (Jiang *et al*. 1992; Qian & Law 1997), to incorporate the influence of ambient gases, the ambient pressure p is usually included to describe the collision dynamics. Nonetheless, because p is not a dimensionless number, a variety of gas types is also frequently considered to fully understand the effect of ambient gases. On outcomes, the previous study (Qian & Law 1997) has shown that ambient gas mainly affects Regime BO, while its effect on other regimes (CO, SS and RES) is relatively weak. Specifically, in a wide range of ambient gas pressures, the boundaries between Regimes CO, SS and RES only alter slightly, while the boundaries between Regime BO and other outcomes can change dramatically. For β_{max}, Jiang *et al*. (1992) have pointed out that the work on ambient gas by droplets is negligible compared with the viscous dissipation inside the droplets, so it is believed that the ambient gas does not affect β_{max}. Another piece of evidence is that the head-on transition between Regimes CO and RES, which is strongly dependent on the viscous dissipation during head-on collisions, does not change significantly over a wide pressure range of 100 to 800 kPa (Qian & Law 1997). Therefore, the effect of ambient gas at the macroscale can be summarised. For outcomes, the ambient gas mainly affects the boundaries between Regime BO and other regimes, depending on both the type and pressure of the gas. For β_{max}, the effect of ambient gas is not significant. At the nanoscale, the effect of ambient gas on collision dynamics is also important to explore. Here, the discussion of ambient gas below is divided into two groups based on gas pressures, i.e. low ambient gas pressure and high ambient gas pressure.

3.3.1. *Low gas pressure*

In this work, four different liquid models, including SPCE, TIP3P, mW and LJ (for argon), have been used to create different saturated vapour environments. Among the three water models (SPCE, TIP3P and mW), TIP3P can satisfactorily reproduce the saturated vapour pressure of water in experiments (3.5 kPa at no curvature), while mW significantly underestimates the saturated vapour pressure (close to a vacuum). The saturated vapour pressure of SPCE is intermediate between that of TIP3P and mW. The LJ model creates a saturated vapour pressure of up to 79 kPa for argon (at no curvature) (Yaguchi *et al*. 2010). In addition to these scenarios, a system containing mW water droplets, filled with argon gas, is also considered to produce a vapour pressure that is the same as the saturated vapour pressure of water in experiments. In summary, a range of gas pressures from approximately 0 (mW) to 79 kPa (Ar) and different types of gases (mW water vapour,

SPCE water vapour, TIP3P water vapour, and argon vapour and gas) are tested in the low ambient pressure range. Here, the pressure range is characterised by vapour pressures at no curvature, but to avoid ambiguity, it is worth noting that the Kelvin effect can occur according to the diameters of droplets. Controlling Oh and B of these droplets and comparing their β_{max} over a wide range of Weber numbers, it is found that when the values of the dimensionless numbers (We, Oh, B) are the same, they have almost the same values of β_{max}, independent of the ambient gas type and ambient gas pressure, as shown in figure S1. Therefore, for collisions at low ambient gas pressures ($p < 79$ kPa), it can be believed that the collision dynamics is still governed by the dimensionless numbers (We, Oh, B). This is also consistent with the results of macroscale studies. Therefore, the conclusions from §§ 3.1 and 3.2 are equally applicable to the collision dynamics at low gas pressures.

3.3.2. *High gas pressure*

When exposed to high ambient gas pressures, nanodroplets appear to show different dynamics from that of macroscale droplets. For macroscale collisions, Qian & Law (1997) have reported that with increasing p, the area of Regime BO in phase diagrams increases, and the other regimes can be significantly suppressed. This is because the correspondingly increasing density of the gas cushion entrapped between two approaching droplets hinders them from merging. However, the extremely small scale of nanodroplets renders the stable gas cushion difficult to form, so the gas between them is more likely to be squeezed out, making the bouncing almost impossible. A recent study (Zhang, Jiang & Luo 2016) indicated that bouncing can still take place for nanodroplets if the gas pressure is increased to 270 kPa. However, from the bouncing snapshots reported by them, the nanodroplets stop approaching due to the existence of a gas cushion. After that, the two nanodroplets are suspended in gas environments. In traditional bouncing, when two droplets approach each other, the gas cushion between droplets is compressed with high pressure, resulting in the flattening of the droplets and hence the energy conversion from kinetic energy to surface energy; subsequently, when the initial kinetic energy is exhausted, the stored surface energy is released to induce the bouncing of droplets away from each other. Therefore, the bouncing reported by Zhang *et al*. (2016) is different from traditional bouncing. Within this context, whether traditional bouncing can take place at the nanoscale should be further verified.

In addition to Regime BO, the viscous dissipation during head-on collisions is also concerned at the nanoscale. The macroscale study (Jiang *et al*. 1992) indicated that the work by droplets on gas can be negligible compared with the viscous dissipation inside the droplets. However, Zhang & Luo (2019) reported that at each We, β_{max} significantly decreases with increasing p. Although they ascribed this to the gas cushion effect, the relationship between energy dissipation and the gas cushion effect has not been quantitatively described.

The phase diagrams at $p = 120$ and 450 kPa at 300 K, with $\rho_g = 1.42$ and 6.82 kg m^{-3}, respectively, are shown in figure 11. It is found that the increased gas pressure does not significantly affect the boundary between Regimes CO and SS, and Regime BO still does not occur. For nanodroplets, the gas environment may not be a continuum. According to the kinetic theory of gases, the mean free path of gas atoms can be calculated by $\lambda = k_B T/(2^{1/2}\pi d^2 p)$, and λ is obtained as 60.6 and 16.2 nm at $p = 120$ and 450 kPa, respectively, where k_B is the Boltzmann constant and $d = 3.58$ Å is the effective diameter of argon atoms (Guggenheim & McGlashan 1960). Therefore, the Knudsen numbers ($Kn = \lambda/D_0$) for these two gas environments are 6.06 at $p = 120$ kPa and 1.62 at 450 kPa. Such large values of Kn indicate that the gas environments are in the transitional flow

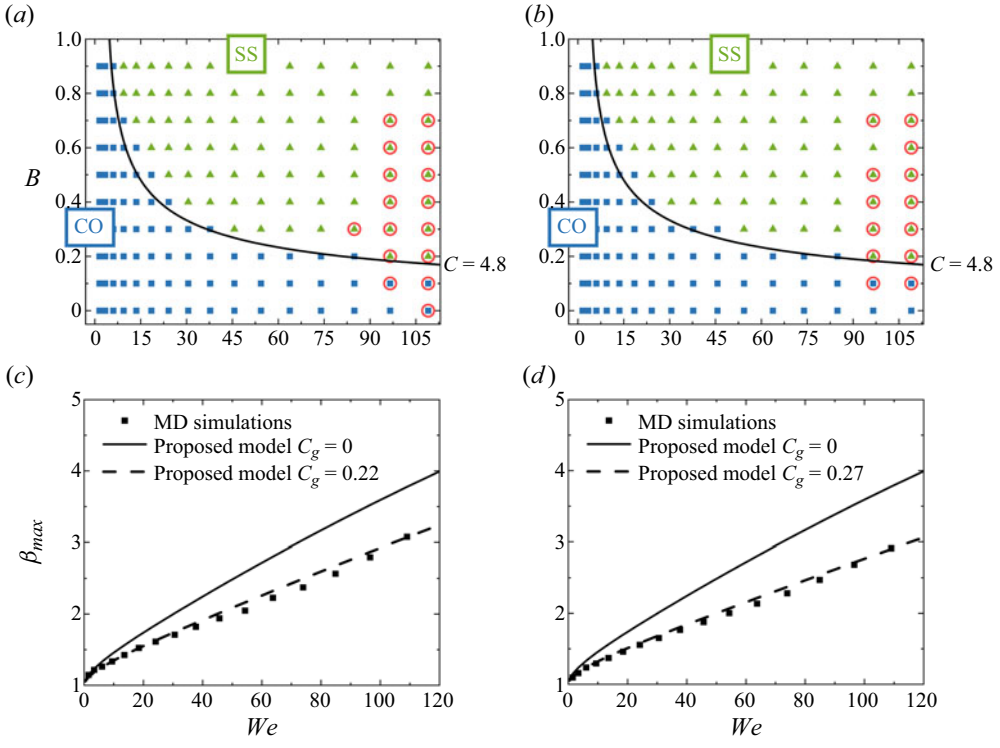

Figure 11. (*a*,*b*) Phase diagrams at gas pressures of (*a*) 120 and (*b*) 450 kPa. The comparison of β_{max} between MD simulation results and theoretical predictions at gas pressures of (*c*) 120 and (*d*) 450 kPa.

regime, and importantly, strong rarefaction effects emerge (Gad-el-Hak 1999). Because stretching separation frequently takes place at a relatively high value of off-centre distance, the viscous drag force for each nanodroplet can be approximately treated as that for a single nanodroplet moving in gas environments. At these large *Kn* of 1.62 and 6.06, the rarefaction effect has been strong, which significantly reduces viscous drag force. Therefore, it can be expected that the reduced viscous drag does not show a remarkable change when *Kn* decreases from 6.06 to 1.62. Accordingly, when gas pressure increases from 120 to 450 kPa, the boundary between Regimes CO and SS is almost not altered, as shown in figure 11(*a*,*b*).

Zarin (1970) and Loth (2008) proposed that when the particle Reynolds number ($Re_p = \rho_g D_0 V_0/\mu_g$) is lower than 45, the motion of particles (i.e. nanodroplets) is dominated by the rarefaction effect but not by the compressibility effect. For argon, $\rho_g = 1.42$ and 6.82 kg m^{-3} at $p = 120$ and 450 kPa, respectively; μ_g is not sensitive to p when $p < 10$ Mpa (Trappeniers *et al*. 1964) and equals 22.5 μPa s (Berg & Burton 2012). Using $D_0 = 10$ nm and the maximum impact velocity ($V_{0,max} = 850$ m s^{-1}), the maximum Re_p is 2.58, which is far lower than 45 and shows the dominant rarefaction effect. Owing to the large Knudsen numbers and the dominant rarefaction effect, the stable gas cushion cannot form at the nanoscale, which is responsible for no Regime BO being observed at the nanoscale.

Compared with Regime SS, both Regime SH and the hole regime are remarkably suppressed, and especially Regime SH does not occur in the tested *We* range. More importantly, the maximum spreading factors are also reduced when increasing gas

pressures, as shown in figure 11(*c*,*d*). During head-on collisions, the gas molecules between two approaching nanodroplets will be squeezed out, leading to the viscous drag force for head-on nanodroplets being larger than that for a single nanodroplet moving in the same gas environment, and the viscous drag force will continuously increase with the distance between two nanodroplets decreasing. More importantly, the increase in viscous drag force can be strengthened by decreasing *Kn* (Chun & Koch 2005). As a result, when gas pressure increases from 120 to 450 kPa (i.e. *Kn* decreases from 6.06 to 1.62), the reduction in the maximum spreading factor is more significant, as shown in figure 11(*c*,*d*).

In these high-pressure environments, part of the initial kinetic energy is additionally consumed due to the viscous drag force caused by the displacement of gas molecules by nanodroplets. Here, the consumed kinetic energy by the viscous drag force is added to (3.20) by an additional energy term scaling with the initial kinetic energy, i.e. $C_g(\rho D_0^3 V_0^2/12)$, leading to the simply modified model of β_{max} as

$$\frac{1}{3}\beta_{max}^2+\frac{2}{3}\frac{1}{\beta_{max}}-1=(1-C_g)\frac{We}{12}-4C_{vf}We^{1/2}Oh\left(1-\frac{1}{\beta_{max}}\right), \tag{3.21}$$

where C_g is a fitting parameter. When gas pressure increases (*Kn* decreases), the displaced number of gas molecules increases and the viscous drag force is enhanced, so C_g should be positively related to p. Using $C_g=0.22$ at $p=120$ kPa and 0.27 at $p=450$ kPa, the modified model can well fit the data on collisions in high gas pressure environments. This agreement indicates the effectiveness of the insight that the displacement of gas molecules by nanodroplets consumes part of the initial kinetic energy and the viscous drag force increases with decreasing *Kn* during head-on collisions at the nanoscale.

4. Conclusions

In this study, the binary nanodroplet collision dynamics is studied through MD simulations, aiming to reveal outcome regimes and estimate the viscous dissipation during spreading. Simulations are implemented for droplet diameters (6, 8 and 10 nm) in wide ranges of *We* (1–109) and *B* (0–0.9). In addition, the effect of gas pressures (vacuum, 120 and 450 kPa) is also discussed.

In a vacuum, outcome regime diagrams are constructed in a *We*–*B* coordinate system, where three outcomes, coalescence (CO), stretching separation (SS) and shattering (SH), are successfully identified, whereas bouncing (BO), reflexive separation (RES) and rotational separation (ROS), which have been extensively reported for macroscale collisions, are not observed. This result is explained by the fact that the reduction in droplet sizes increases *Oh* significantly, thereby enhancing the viscous effect. In other words, natural high-viscosity nanodroplets are responsible for the non-observed three outcomes in the tested *We* range in this work. In addition, holes are generated for the observed outcomes in a high-*We* range, and, as an intermediate outcome, their formation is attributed to the vibration-induced rupture of the nanoscale film and the action of thermal fluctuations. The splashing rims in Regime SH are ascribed to the Rayleigh–Taylor instability, which is proven by comparing the finger numbers between MD simulations and theoretical results.

Since Regimes CO and SS occupy most regions of phase diagrams, the focus is subsequently placed on the development of the boundary equation between them. The boundary equation is established based on the criterion that the residual off-centre kinetic energy after overcoming the viscous dissipation can still be larger than the surface energy required for triggering the stretching separation. As a result, the estimation of viscous dissipation becomes a determinant. The flow feature extracted from MD simulations shows

that the extensional flow assumption well fits the velocity gradient distributions in both impact and spreading directions. Based on this, viscous dissipation is calculated, and the ratio (α) of the viscous dissipation during spreading to the initial kinetic energy is estimated for various *We* and *Oh*. The result shows that the ratio is independent of *We* and remains constant at a fixed *Oh*; it increases with *Oh* due to the enhanced viscous effect. Using the obtained *Oh*-dependent ratio, the boundary equation successfully predicts the boundaries between Regimes CO and SS for both nanoscale and macroscale binary droplet collisions. It is worth noting that, owing to intricate viscous dissipation mechanisms, the relationship between α and *Oh* is still an issue of concern in the cross-over regime for macroscale binary droplet collisions. Therefore, the estimation of viscous dissipation in this work also provides a possible insight into understanding the energy conversion of macroscale collisions when the viscous force is no longer negligible.

Another contribution of this work is that a model of the maximum spreading factor is developed for head-on binary nanodroplet collisions based on the estimation of viscous dissipation. The model shows good agreement with almost all available data on β_{max}. In addition, based on similarity, this model is also extended to predict the maximum spreading factor for the impact of a nanodroplet on solid surfaces. A thorough test indicates that with a constant fitting parameter of $C_{vf} = V_s/V_0 = 0.85$, the model fits MD data on solid surfaces with θ ranging from 73° to 180° satisfactorily. More importantly, this model also shows good agreement with the available experimental data on nanodroplets impacting solid surfaces in an inkjet printing process.

Finally, binary nanodroplet collisions are also examined at two gas pressures of 120 and 450 kPa. The result shows that bouncing is not triggered even if the pressure increases to 450 kPa. This unexpected result indicates that there is a different pressure effect between macroscale and nanoscale collisions. A possible cause of the absence of Regime BO is that the rarefaction effect is dominant instead of the compressibility effect. This rarefaction effect also contributes to the fact that the boundary between Regimes CO and SS is not significantly altered. However, the maximum spreading factor of merged nanodroplets is remarkably suppressed at high gas pressures because the displacement of gas molecules by nanodroplets consumes part of the initial kinetic energy. To test this insight, a kinetic energy term consumed by gas is added to the model of β_{max}. The modified model can satisfactorily fit MD results of β_{max} at different pressures ($p = 120$ and 450 kPa).

Supplementary material. Supplementary material is available at https://doi.org/10.1017/jfm.2023.1069.

Funding. This study was partially supported by the State Key Program of National Natural Science of China (no. 51936004) and Science Fund for Creative Research Groups of the National Natural Science Foundation of China (no. 51821004).

Declaration of interests. The authors report no conflict of interest.

Author ORCIDs.
Shao-Fei Zheng http://orcid.org/0000-0003-0539-8639;
Duu-Jong Lee http://orcid.org/0000-0002-5111-2390;
Xiao-Dong Wang http://orcid.org/0000-0002-4533-6734.

Appendix A. Calculation of the off-centre factor (P_o)

The off-centre factor represents the volume of one in two droplets out of the projection of the other one, as shown in figure 12. The values of P_o at various B are obtained numerically, as shown in figure 13. With the help of a polynomial fitting procedure, the

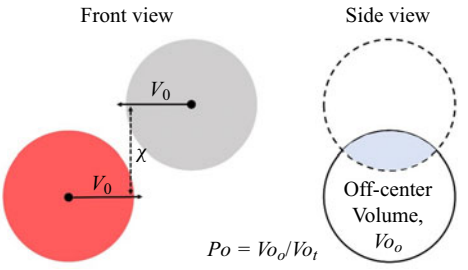

Figure 12. Front and side views of binary droplet collisions, where the off-centre volume (Vo_o) and the total volume of one droplet (Vo_t) are shown schematically.

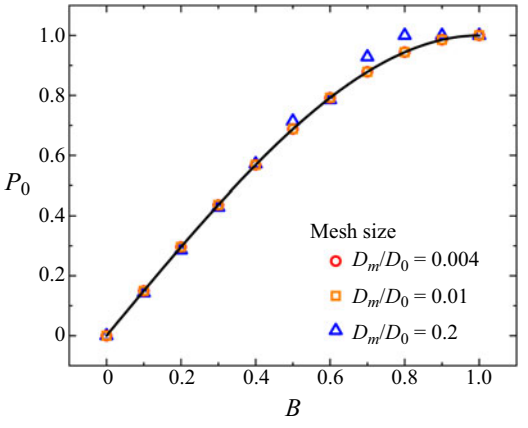

Figure 13. Numerical results of P_o at various B with different numerical mesh sizes (D_m/D_0) of 0.004, 0.01 and 0.2, where D_m denotes the side length of each cubic mesh. Using polynomial fitting, the expression of P_o is obtained as $P_o = -0.5B^3 + 1.5B$.

expression of P_o is determined as

$$P_o = -0.5B^3 + 1.5B. \tag{A1}$$

This expression shows good agreement with the numerical results. Since the parameter P_o is controlled only by the off-centre parameter (B), the expression is universal.

References

Al-Dirawi, K.H., Al-Ghaithi, K.H., Sykes, T.C., Castrejon-Pita, J.R. & Bayly, A.E. 2021 Inertial stretching separation in binary droplet collisions. *J. Fluid Mech.* **927**, A9.

Allen, R.F. 1975 The role of surface tension in splashing. *J. Colloid Interface Sci.* **51**, 350–351.

Bach, G.A., Koch, D.L. & Gopinath, A. 2004 Coalescence and bouncing of small aerosol droplets. *J. Fluid Mech.* **518**, 157–185.

Berg, R.F. & Burton, W.C. 2012 Noble gas viscosities at 25°C. *Mol. Phys.* **111**, 195–199.

Chaitanya, G.S., Sahu, K.C. & Biswas, G. 2021 A study of two unequal-sized droplets undergoing oblique collision. *Phys. Fluids* **33**, 022110.

Chun, J. & Koch, D.L. 2005 A direct simulation Monte Carlo method for rarefied gas flows in the limit of small Mach number. *Phys. Fluids* **17**, 107107.

Faeth, G. 1977 Current status of droplet and liquid combustion. *Prog. Energy Combust. Sci.* **3**, 191–224.

Gad-el-Hak, M. 1999 The fluid mechanics of microdevice – the Freeman scholar lecture. *J. Fluids Engng* **121**, 5–33.

Galliker, P., Schneider, J., Eghlidi, H., Kress, S., Sandoghdar, V. & Poulikakos, D. 2012 Direct printing of nanostructures by electrostatic autofocussing of ink nanodroplets. *Nat. Commun.* **3**, 890.

GLASSCOTT, M.W., PENDERGAST, A.D., GOINES, S., BISHOP, A.R., HOANG, A.T., RENAULT, C. & DICK, J.E. 2019 Electrosynthesis of high-entropy metallic glass nanoparticles for designer, multi-functional electrocatalysis. *Nat. Commun.* **10**, 2650.

GUGGENHEIM, E.A. & MCGLASHAN, M.L. 1960 Interaction between argon atoms. *Proc. R. Soc.* A – *Math. Phys.* **255**, 456–476.

HENNEQUIN, Y., AARTS, D., VAN DER WIEL, J.H., WEGDAM, G., EGGERS, J., LEKKERKERKER, H.N.W. & BONN, D. 2006 Drop formation by thermal fluctuations at an ultralow surface tension. *Phys. Rev. Lett.* **97**, 244502.

HUANG, K.L., PAN, K.L. & JOSSERAND, C. 2019 Pinching dynamics and satellite droplet formation in symmetrical droplet collisions. *Phys. Rev. Lett.* **123**, 234502.

JACOBSON, L.C., KIRBY, R.M. & MOLINERO, V. 2014 How short is too short for the interactions of a water potential? Exploring the parameter space of a coarse-grained water model using uncertainty quantification. *J. Phys. Chem.* B **118**, 8190–8202.

JIANG, Y., UMEMURA, A. & LAW, C. 1992 An experimental investigation on the collision behaviour of hydrocarbon droplets. *J. Fluid Mech.* **234**, 171–190.

JOSSERAND, C. & THORODDSEN, S.T. 2016 Drop impact on a solid surface. *Annu. Rev. Fluid Mech.* **48**, 365–391.

KIRKWOOD, J.G. & BUFF, F.P. 1949 The statistical mechanical theory of surface tension. *J. Chem. Phys.* **17**, 338–343.

KOPLIK, J., BANAVAR, J.R. & WILLEMSEN, J.F. 1988 Molecular dynamics of Poiseuille flow and moving contact lines. *Phys. Rev. Lett.* **60**, 1282–1285.

LI, B.X., LI, X.H. & CHEN, M. 2017 Spreading and breakup of nanodroplet impinging on surface. *Phys. Fluids* **29**, 012003.

LI, X.H., ZHANG, X.X. & CHEN, M. 2015 Estimation of viscous dissipation in nanodroplet impact and spreading. *Phys. Fluids* **27**, 052007.

LIU, M. & BOTHE, D. 2016 Numerical study of head-on droplet collisions at high Weber numbers. *J. Fluid Mech.* **789**, 785–805.

LOTH, E. 2008 Compressibility and rarefaction effects on drag of a spherical particle. *AIAA J.* **46**, 2219–2228.

LV, S.H., XIE, F.F., YANG, Y.R., LEE, D.J., WANG, X.D. & DUAN, Y.Y. 2022 Impact regimes of nanodroplets impacting nanopillared surfaces. *Phys. Rev. Fluids* **7**, 034203.

MOLINERO, V. & MOORE, E.B. 2009 Water modeled as an intermediate element between carbon and silicon. *J. Phys. Chem.* B **113**, 4008–4016.

MOSELER, M. & LANDMAN, U. 2000 Formation, stability, and breakup of nanojets. *Science* **289**, 1165–1169.

PAN, K.L., CHOU, P.C. & TSENG, Y.J. 2009 Binary droplet collision at high Weber number. *Phys. Rev.* E **80**, 036301.

PAN, K.-L., HUANG, K.-L., HSIEH, W.-T. & LU, C.-R. 2019 Rotational separation after temporary coalescence in binary droplet collisions. *Phys. Rev. Fluids* **4**, 123602.

PLANCHETTE, C., HINTERBICHLER, H., LIU, M., BOTHE, D. & BRENN, G. 2017 Colliding drops as coalescing and fragmenting liquid springs. *J. Fluid Mech.* **814**, 277–300.

QIAN, J. & LAW, C.K. 1997 Regimes of coalescence and separation in droplet collision. *J. Fluid Mech.* **331**, 59–80.

SOMMERFELD, M. & KUSCHEL, M. 2016 Modelling droplet collision outcomes for different substances and viscosities. *Exp. Fluids* **57**, 187.

SOMMERFELD, M. & PASTERNAK, L. 2019 Advances in modelling of binary droplet collision outcomes in sprays: a review of available knowledge. *Intl J. Multiphase Flow* **117**, 182–205.

STEVANOVIC, M.M. 1984 Evaluation of the temperature dependence of vapour pressure for silicon and germanium. *Thermochimi. Acta* **77**, 167–176.

STILLINGER, F.H. & WEBER, T.A. 1985 Computer simulation of local order in condensed phases of silicon. *Phys. Rev.* B **31**, 5262–5271.

TRAPPENIERS, N. J., BOTZEN, A., VAN DEN BERG, H. R. & VAN OOSTEN, J. 1964 The viscosity of Neon between 25°C and 75°C at pressures up to 1800 atmospheres. Corresponding states for the viscosity of the noble gases up to high densities. *Physica* **30**, 985–996.

VÁZQUEZ-QUESADA, A., MAHMUD, A., DAI, S., ELLERO, M. & TANNER, R.I. 2017 Investigating the causes of shear-thinning in non-colloidal suspensions: experiments and simulations. *J. Non-Newtonian Fluid* **248**, 1–7.

WANG, Y.B., WANG, Y.F., GAO, S.R., YANG, Y.R., WANG, X.D. & CHEN, M. 2020*a* Universal model for the maximum spreading factor of impacting nanodroplets: from hydrophilic to hydrophobic surfaces. *Langmuir* **36**, 9306–9316.

WANG, Y.B., WANG, Y.F., WANG, X., ZHANG, B.X. & CHEN, M. 2021*b* Splash of impacting nanodroplets on solid surfaces. *Phys. Rev. Lett.* **6**, 094201.

WANG, Y.-B., WANG, Y.-F., YANG, Y.-R., WANG, X.-D. & CHEN, M. 2021*a* Spreading time of impacting nanodroplets. *J. Phys. Chem.* B **125**, 5630–5635.

WANG, Y.-F., WANG, Y.-B., HE, X., ZHANG, B.-X., YANG, Y.-R., WANG, X.-D. & LEE, D.-J. 2022*a* Retraction dynamics of low-viscosity nanodroplets: from hydrophobic to hydrophilic surfaces. *J. Mol. Liq.* **355**, 118963.

WANG, Y.-F., WANG, Y.-B., HE, X., ZHANG, B.-X., YANG, Y.-R., WANG, X.-D. & LEE, D.-J. 2022*b* Scaling laws of the maximum spreading factor for impact of nanodroplets on solid surfaces. *J. Fluid Mech.* **937**, A12.

WANG, Y.-F., WANG, Y.-B., XIE, F.-F., LIU, J.-Y., WANG, S.-L., YANG, Y.-R., GAO, S.-R. & WANG, X.-D. 2020*b* Spreading and retraction kinetics for impact of nanodroplets on hydrophobic surfaces. *Phys. Fluids* **32**, 092005.

WILDEMAN, S., VISSER, C.W., SUN, C. & LOHSE, D. 2016 On the spreading of impacting drops. *J. Fluid Mech.* **805**, 636–655.

WILLIS, K. & ORME, M. 2003 Binary droplet collisions in a vacuum environment: an experimental investigation of the role of viscosity. *Exp. Fluids* **34**, 28–41.

XIE, F.F., LV, S.H., YANG, Y.R. & WANG, X.D. 2020 Contact time of a bouncing nanodroplet. *J. Phys. Chem. Lett.* **11**, 2818–2823.

YAGUCHI, H., YANO, T. & FUJIKAWA, S. 2010 Molecular dynamics study of vapor-liquid equilibrium state of an argon nanodroplet and its vapor. *J. Fluid Sci. Technol.* **5**, 180–191.

YIN, Z., SU, R., ZHANG, W., ZHANG, C., XU, H., HU, H., ZHANG, Z., HUANG, B. & LIU, F. 2021 Binary collisions of equal-sized water nanodroplets: molecular dynamics simulations. *Comput. Mater. Sci.* **200**, 110774.

ZARIN, N.A. 1970 Measurement of non-continuum and turbulence effects on subsonic sphere drag. *NASA* No. NASA-CR-1585.

ZHANG, Y., SPRITTLES, J.E. & LOCKERBY, D.A. 2019 Molecular simulation of thin liquid films: thermal fluctuations and instability. *Phys. Rev.* E **100**, 023108.

ZHANG, Y.R., JIANG, X.Z. & LUO, K.H. 2016 Bounce regime of droplet collisions: a molecular dynamics study. *J. Comput. Sci.* **17**, 457–462.

ZHANG, Y.R. & LUO, K.H. 2019 Regimes of head-on collisions of equal-sized binary droplets. *Langmuir* **35**, 8896–8902.

ZHANG, Y.R., ZHAO, Z., LUO, K.H. & SHI, B. 2021 Size effects on dynamics of nanodroplets in binary head-on collisions. *J. Mol. Liq.* **341**, 117383.